Jesús Lloredo Fernández

Joint phase unwrapping for multi-frequency SAR Interferometry

Master's Thesis in Electronic Engineering

German Aerospace Center (DLR)
Microwaves and Radar Institute
École Nationale Supérieure de l'Électronique et de ses Applications (ENSEA)
Chair for Information Processing and System Research Lab

Title:	Joint phase unwrapping for multi-frequency SAR Interferometry
Author:	Jesús Lloredo Fernández
Supervisor ENSEA:	Dr. Sylvain Reynal
Supervisor DLR:	Muriel Aline Pinheiro
Date:	August 12, 2014

Abstract

An important step in the interferometric processing chain is the phase unwrapping, which transforms the ambiguous phase (wrapped in the interval -/+ 180°) in an unambiguous phase. This unambiguous phase can then be used for the computation of the scene height model. Standard phase unwrapping methods work with data from a single frequency and a single baseline at a time. The unwrapping becomes extremely challenging for data with small height of ambiguity (HoA), which is usually the case when working with high frequencies and large baselines. The use of multichannel information can help to solve the ambiguities, improving the unwrapping results. However, for airborne repeat-pass InSAR data, the presence of uncompensated residual motion errors usually affects the efficiency of multibaseline approaches. For systems capable of acquiring data simultaneously in different frequency bands, as is the case of the F-SAR of DLR, multifrequency approaches can be explored to cope with the residual errors issue. In this thesis, different unwrapping algorithms are evaluated for the unwrapping of data with small height of ambiguity. Furthermore, methods to jointly unwrap interferograms from multifrequency acquisitions in a robust manner are analyzed.

KEYWORDS: SAR, interferometry, phase unwrapping, multi-channel, optimization

Outline of the Thesis

CHAPTER 1: INTRODUCTION

In this chapter there is a brief description of the SAR (Synthetic Aperture Radar). Then, this introduction focuses more on the field studied in the thesis with the review of the SAR Interferometry, presenting some of the InSAR systems managed by the DLR. This review continues with the proposal of the *phase unwrapping* problem crucial in the Earth height reconstruction process.

CHAPTER 2: STATE OF THE ART

In this chapter there is a presentation of the *phase unwrapping* problem complemented by a review of the different existing unwrapping algorithms which are used to solve it. Secondly, the STEP processor is presented followed by a detailed explanation of its already implemented unwrapping methods. At the end there are presented some Statistical Multi-Channel methods for the phase unwrapping process.

CHAPTER 3: EXPERIMENTS AND RESULTS

Here it is found the the main part of the thesis, the developed joint phase unwrapping algorithm. At the beginning, a simple comparison of the existing STEP unwrapping algorithms is done to give thought to what of them would be better for a joint phase approach. Then there is a presentation of the two developed approaches for the joint unwrapping for multi-frequency acquisitions: one based on the frequency extension of the Region Growing algorithm and the second based on statistical minimizations.

CHAPTER 4: CONCLUSION

Finally, an evaluation of the improvements achieved in the new methods is given here. The benefits and drawbacks are pointed out, comparing its performance to that one of the previous methods. Additionally, the possible future work is described here.

Contents

List of Figures

.

1 Introduction

1.1 SAR: Synthetic Aperture Radar

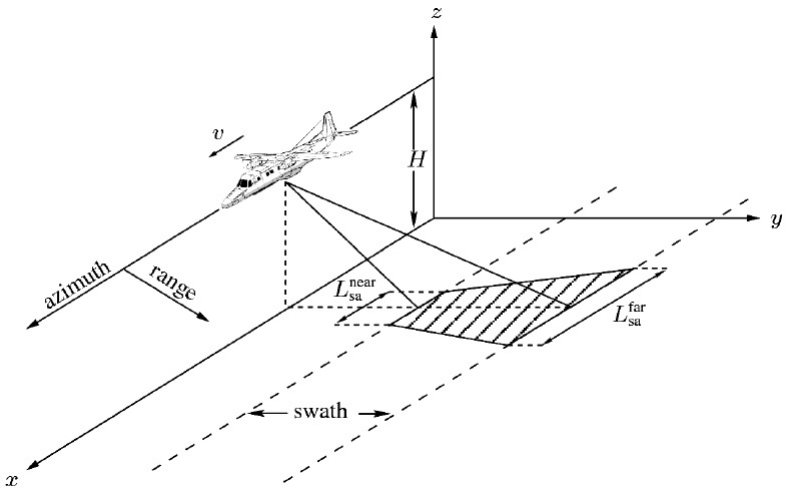

Figure 1.1: SAR schema in three dimensions[1]

A general definition of RADAR (Radio Detection and Ranging) is a detection system which uses radio waves to determine different parameters of an object like its position or its speed. We have two different mechanisms of radar, the active radar and the passive radar. The active one is the most common. Its principle of operation is the antenna emission of a radio wave and the antenna reception of the echoed signals proceeding from the wave reflection on the encountered objects. On the other hand, we have the passive radar which just collects the energy reflected or emitted form a surface. It does not emit anything. Radar systems are based on either of these technologies, or even a combination of both.

The Synthetic Aperture Radar (SAR) systems are active imaging systems used for the creation of high resolution images acquired at large distances. The system itself is composed of an airplane or satellite where a radar has been incorporated. This radar is fixed during the system movement of the platform that follows a straight line. This option is called "stripmap" mode. This is the most used mode but there are several ones. We have the "scansar" mode in which the antenna beam is periodically changed or the "spotlight" mode where the antenna is steered during the acquisition process [1]. This system moves, with respect to the target, with a constant velocity v and at a height h.

The SAR systems send pulses and receives the backscatered echoes. These pulses have

certain duration at a certain pulse repetition frequency (PRF). As might be expected, the PRF must fulfill the Nyquist sampling theorem. Once the backscattered echoes are received, they are processed with certain sampling and filtered until the creation of a matrix called the *raw-data matrix*. The process of the echoes will be explained more in detail in the section. At the end of the whole process (emission, detection and data treatment), a high resolution reflectivity map of the studied area is created.

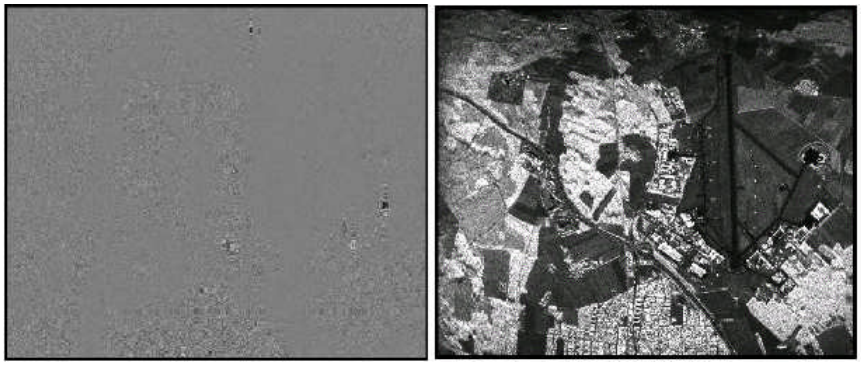

Figure 1.2: Raw data and its corresponding reflectivity map.[2].

There are multiple characteristics that define the SAR system and its performance. A good schema of it i shown in (Fig. 1.1). First of all, we differentiate two coordinates: the azimuth direction and the slant-range direction. The azimuth direction is the flight one, whereas the range direction is the propagation direction of the pulses, which is orthogonal to the azimuth. The antenna of the radar and its radiation is characterized by an azimuth beamwidth θ_{az} and the elevation beamwidth. The elevation beamwidth θ_e corresponds to the beamwidth in the ground range or the swath size. This ground range is just the slant-range projection on the ground [2].

With the azimuth beamwidth θ_{az} and taking into account the instant when the target enters into the beamwidth and the instant when it leaves it, we calculate the length of the synthetic aperture L_{sa}.

$$L_{sa} = 2r_o \cdot tan(\theta_{az}/2) \tag{1.1}$$

Where r_o is the minimum distance from the platform to the target.

Also with the azimuth beamwidth θ_{az} we calculate the azimuth resolution. This resolution defines the minimum distance between targets in the azimuth direction that permits to detect both targets.

$$\delta_{az} = r_o \cdot \theta_{az} \tag{1.2}$$

As it can be seen in this equation, to have a good antenna aperture and hence a good resolution we need really small azimuth beamwidth. This reduction has obviously some physical limits, so the resolution improvement should rely in more factors. The high resolution is

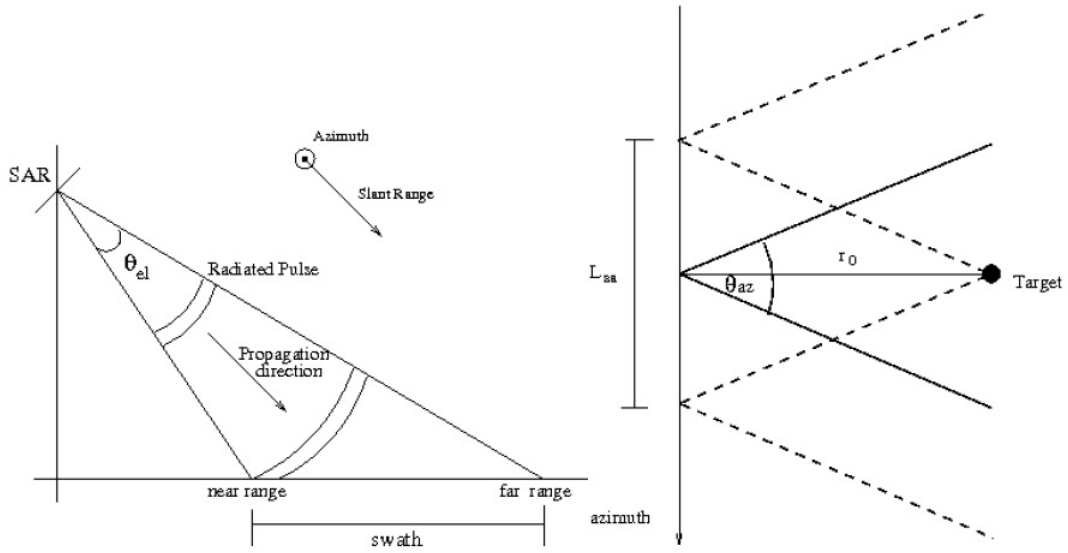

Figure 1.3: SAR schema in 2 dimension[3].

achieved with a long antenna in time together with the movement of the aircraft. Besides, the echoes of the targets must be combined in a coherent way. Therefore, the azimuth resolution is going to be defined by the azimuth bandwidth. And to calculate this bandwidth we have to consider the Doppler effect, because there is a relative movement between the target and the platform. The maximum Doppler frequency is received from the edges of the antenna beamwidth.

$$f_{max} = \frac{1}{2\pi} \cdot \frac{d(2 \cdot \frac{2\pi}{\lambda}\mathbf{r_{max}})}{dt} = \frac{2\mathbf{v_{max}}}{\lambda} = \frac{2v}{\lambda} \cdot \sin(\pm\frac{\theta_{az}}{2}) \tag{1.3}$$

Where v is the velocity of the platform and 2 comes from the round trip way. Now, the bandwidth in azimuth is calculated straightforward

$$B_{az} = \frac{4v}{\lambda} \cdot \sin(\frac{\theta_{az}}{2}) \tag{1.4}$$

As we are working with complex images, the Nyquist criteria mentioned before implies that the PRF has to be at least as the azimuthal bandwith

$$PRF_{min} = B_{az} = \frac{4v}{\lambda} \cdot \sin(\frac{\theta_{az}}{2}) \approx \frac{2v}{L_{ant}} \tag{1.5}$$

Considering a proportional weighting window α_w that provides accuracy in the processing, the resolution in the azimuth direction can be defined as

$$\delta_{az} = \alpha_w \frac{v}{B_{az}} \approx \alpha_w \frac{L_{az}}{2} \tag{1.6}$$

Observe that the azimuth resolution is not influenced by the range distance, which allows a better performance in SAR systems, even when working at high distances from the earth surface as is the case of space-borne missions [3].

On the other hand, to locate the targets in range, we need the delay in time corresponding to the round trip of the pulse.

$$\tau_d = \frac{2 \cdot r(t; r_o)}{c} \tag{1.7}$$

As it can be remarked in the formula, the range distance to the target r depends on the azimuthal time which is related to the flight position. r_o is the minimum distance from the platform to the target that is achieved when the target is in the center of the beamwidth (for zero squint geometries).

Taking this into account, the duration of the transmitted pulse τ_p is going to determine the resolution in range (1.8). This resolution is the minimum distance in range between targets permitting the identification of both targets.

$$\delta_e = \frac{c \cdot \tau_p}{2} \tag{1.8}$$

In order to obtain better resolutions, phase coded pulses like the chirp signal are used. These pulses have the advantage of integrating the energy period of the target so that after matching filtering, this energy is compressed at its range position.

$$\delta_e = \alpha_w \frac{c}{2 \cdot B_{rg}} \tag{1.9}$$

At present, resolutions of around 1 meter or less are achievable in *stripmap* mode, and can be further decreased using for example *spotlight* acquisitions.

1.1.1 SAR applications

The Synthetic Aperture Radars (SAR) are the main instruments for the earth surface study. This microwave technique has been of great utility for topographic mapping but also for other applications:

- Cartography
- Earthquakes and natural hazards studies
- Biomass and vegetation estimation
- Ocean current measurement
- Soil moisture mapping
- Glaciar motion detection

1.2 SAR Processing

The *raw-data matrix* obtained with the backscattered echoes has to be processed in order to focus the information of each target at a certain position (t_o, r_o). With the intention of maximizing the resolution it is necessary to compress the data in the two dimensions, azimuth and range.

First of all, before showing any equation, it is important to differentiate between two times, the *slow* time, t, and the *fast* time, τ. The slow time corresponds to the azimuthal time and the fast one corresponds to the time in the range time axis. After this note, the transmitted and received pulses are given by

$$s_t(\tau) = s(\tau) \cdot exp(j2\pi f_c \tau)) \tag{1.10}$$

$$s_r(\tau) = B \cdot s(\tau - \tau_d) \cdot exp(j2\pi f_c(\tau - \tau_d))) \tag{1.11}$$

B is a term including the attenuation, gains and reflectivity effects. s is the envelope of the emitted pulse, f_c the frequency of the pulse and τ_d is the time delay between the instant when the pulses is emitted and the instant when it is received. These pulses are band-pass signals and therefore when the backscattered signal arrives to the platform, it passes through a coherent detector. On the other hand, this pulse also depends in the azimuthal time. As the platform moves, the pulse depends on the target position in the antenna beamwidth.

$$s(\tau, t) = \beta \cdot rect(\frac{\tau - \tau_d}{\tau_p}) \cdot rect(\frac{t - t_c}{T_{BM}}) \cdot exp(-j\pi K(\tau - \tau_d)^2) \cdot exp(j2\pi f_c(\tau - \tau_d)) \tag{1.12}$$

K is the *chirp* rate of the transmitted signal. A chirp is a signal in which the frequency increases ('up-chirp') or decreases ('down-chirp') with time, and the advantage of its use is commented in the previous section. With regard to T_{BM}, it is the observation interval related to the antenna footprint at -3dB. Taking into account the round-trip delay in the fast time τ_d and considering that there is no movement in the platform in the pulse trip (*stop and go approximation*), the pulse function can be written in a different way

$$\tau_d = \frac{2 \cdot r(t; r_0)}{c} = \frac{2 \cdot \sqrt{r_o^2 + v^2 \cdot (t - t_0)^2}}{c} \tag{1.13}$$

$$s(\tau, t; t_0) = \beta \cdot rect(\frac{\tau - \tau_d}{\tau_p}) \cdot rect(\frac{t - t_c}{T_{BM}}) \cdot exp(j\pi K(\tau - \frac{2r(t; r_0)}{c})^2 \cdot exp(-j\frac{4\pi}{\lambda} r(t; r_0)) \tag{1.14}$$

t_c is the time when the target is in the center of the beam. t_0 is the time where the target is closest (the *zero-Doppler* position). Considering also the squint angle $\beta(r_0)$, which is the ground-projected angle between the range and azimuth directions, t_c can be defined as follows

$$t_c = t_0 - \frac{r_0}{v} tan(\beta(r_0)) \tag{1.15}$$

And then, the target is observed in the next period of slow time

$$t_c - \frac{T_{BM}}{2} \leq t \leq t_c + \frac{T_{BM}}{2} \tag{1.16}$$

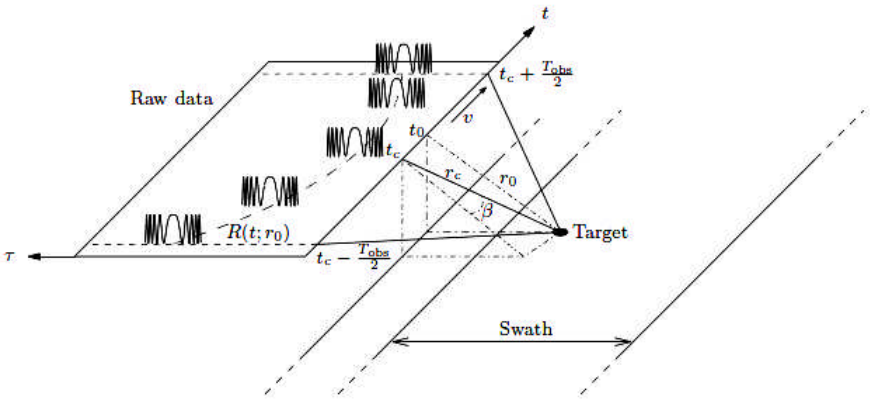

Figure 1.4: SAR acquisition diagram[4].

In the image (Fig. 1.4), the SAR acquisition geometry is displayed and it is remarked that the range distance to the target $r(t; r_0)$ describes an hyperbolic curve. This implies that the locus of the signal varies along the azimuth dimension is known as Range Cell Migration (RCM) [3]. Consequently, the information of a simple target is not stored in a single line but in an hyperbolic one. Furthermore, this curve changes for each target because r_0 is different for each target. The RCM migration is one of the main setbacks for focusing with precision and turns the focusing a 2-D space variant problem. Moreover, the Range Cell Migration (RCMC) depends on the different SAR processors.

Due to the variation of the distance from the target to the platform a synthetic chirp is created in azimuth. By deriving the phase of the last term in (1.14), the frequency variation is found to be

$$f_a = \frac{1}{2\pi} \frac{\partial \phi(t; t_0}{\partial t} = -\frac{2v^2}{\lambda r_0} \cdot (t - t_0) \tag{1.17}$$

being $K_{az} = -\frac{2v^2}{\lambda r_0}$ the chirp rate in azimuth. This frequency is due to the movement between the target and the platform, so it comes from the *Doppler effect*. Now we can write the SAR received signal as follows

$$s(\tau,t;t_0)=\beta\cdot rect(\frac{\tau-\tau_d}{\tau_p})\cdot rect(\frac{t-t_c}{T_{BM}})\cdot exp(j\pi K(\tau-\frac{2r(t;r_0)}{c})^2\cdot exp(-j\frac{4\pi}{\lambda}r_0)\cdot exp(j\pi K_{az}(t-t_0)^2) \tag{1.18}$$

After all these considerations, the first step of the focusing can be attacked, the range compression. For efficiency reasons, this compression is usually carried out in the range frequency domain. Thus, the SAR signal in the range frequency domain is multiplied by the range matched filtered.

$$s_{rc}(f_r,t;r_0)=s(f_r,t;r_0)*H_r^*(f_r) \tag{1.19}$$

$H_r^*(f_r)$ is the matched filter and is just the conjugate of the Fourier transform of the transmitted pulse. Thanks to the matched filtering, there is a correlation between the range line and the transmitted pulse. Finally, the range-compressed signal in time would be

$$s_{rc}(\tau,t;r_0)=F_r^{-1}(s_{rc}(f_r,t;r_0)) \tag{1.20}$$

$$s_{rc}(\tau,t;r_0)=\beta sinc(K\tau_p\cdot(\tau-\frac{2r(t;r_0)}{2}))\cdot rect(\frac{t-t_c}{T_{BM}})\cdot(j\pi K_{az}(t-t_0^2))\cdot exp(-j\frac{4\pi}{\lambda}r_0) \tag{1.21}$$

The next step in the focusing process is the RCMC. Its complexity and variety depend on the SAR processors which will explained later.

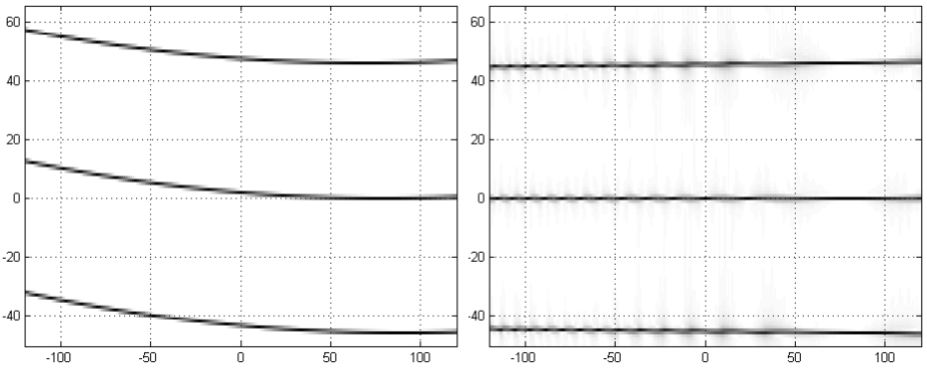

Figure 1.5: RCMC[5].Amplitude of range-compressed data after and before Raw Cell Migration Correction

So, bearing in mind that the RCMC has already been done, the last step is the compression in the azimuth dimension, which is achieved by another matched filtering operation. In this case, the matched filter has a chirp rate K_{az}.

$$H_a=exp(-j\pi K_{az}(t-t_0)^2) \tag{1.22}$$

Finally, the SAR signal compressed both in range and azimuth is

$$s_{rac}(\tau, t; r_0) = \beta sinc(K\tau_p \cdot (\tau - \frac{2r(t; r_0)}{2}))sinc(K_{az}T_{BM} \cdot (t - t_0)) \cdot exp(-j\frac{4\pi}{\lambda}r_0) \quad (1.23)$$

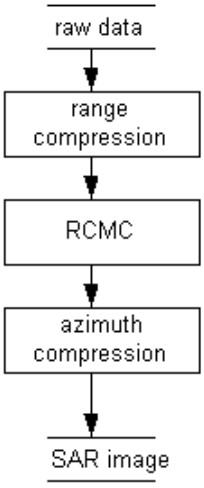

Figure 1.6: Focusing complete process[6].

This compressed signal is a "2-D"' sinc [3]. In order to avoid scatters interferences, the side lobe of the function must be reduced because the *peak side lobe ratio* is quite small, about 13 dB. To achieve this, it is only needed the use of weighting functions such as:

- Hanning window (pulse reduction:-32 dB)
- Hamming window (pulse reduction:-43 dB)
- Blackman window (pulse reduction:-58 dB)
- Gaussian window (pulse reduction:-69 dB)

We can give as example the Hamming window expression which is the most used

$$w(f) = 0.5 + 0.5cos(\frac{\pi}{a}f) \quad (1.24)$$

As it was announced before, there are different processing algorithms that carry out all the previous processing steps. The main element that makes the difference between them is normally the RCMC. For instance, we have two frequency domain processing algorithms, the *Range Doppler Algorithm (RDA)* and the *Chirp Scaling Algorithm (CS)*. Both algorithms work in the range Doppler domain, which means in the frequency domain in range and in azimuth. However each one faces the RCMC in a different way. The RDA relies on interpolation [4].

In this manner, targets separated in azimuth time but with the same r_0 are corrected from the cell migration at the same time. For its part, the CS algorithm uses two phase multiples instead of interpolation [5]. The first one has as goal to equalize the range curvature for all the scatters, and the second multiple attacks the range cell migration correction itself.

Another interesting algorithm is the *w-k algorithm*. This algorithm is not based on approximation so it can deal with the most problematic data with high bandwidth and big squints, which is the weak point of the other processing algorithms. It also corrects the RCM in the range Doppler domain after considering a common reflecting model for all the scatters. Nevertheless this method does not permit a good motion compensation.

One method that gives a good motion compensation and it can deal with difficult scenarios is the Time Domain Back Projection Processing. It must be considered separately from the rest and from the general focusing algorithm presented in this chapter because it does the compression in azimuth in the time domain and it doesn't require a RCMC step. Furthermore, this approach is able to account properly for deviations from the reference tracks. For each pixel, we sum the values of the radar echoes at the range corresponding to the distance between the antenna and the target. This sum is carried out by an integration in the along-track direction(slow time).

$$s_{rac}(\tau, t; r_0) = \int_{-\infty}^{\infty} \beta \cdot p(\tau - \frac{2r(t; r_0)}{c}) \cdot exp(j\frac{4\pi}{\lambda}(r(t; r_0) - r_0))dt \tag{1.25}$$

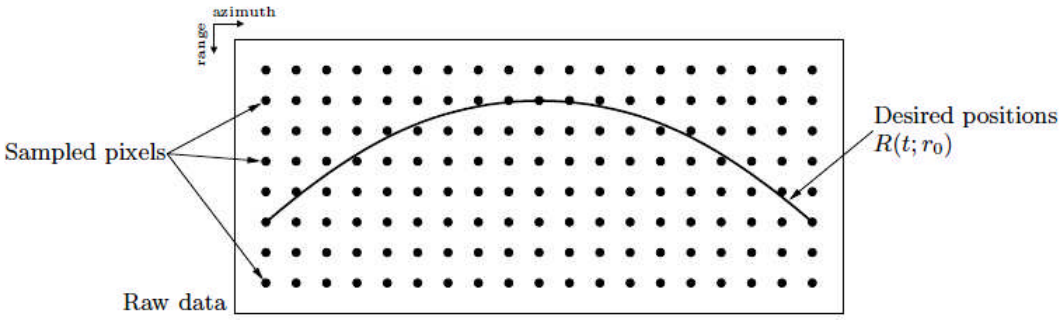

Figure 1.7: Range data hyperbola in azimuth[7].

$p(\tau)$ is the received pulse after the range compression. With the intention of doing a constructive adding process we multiply this pulse by the conjugate of the azimuth modulation term. Although the raw data follows a curve (this curve phenomenon, previously presented is shown again in the Fig. 1.7), the sampling doesn't follow any hyperbola. Therefore, an interpolation in the range sampling is required for each pixel and for each pulse. The echoes have been sampled in discrete time taking into account the Nyquist theorem and thus, the interpolation can be faced with a *weight sinc interpolation*, limiting the integral to the synthetic aperture length L_a where the constructive contributions are found.

$$s_{rac}(\tau, t; r_0) = \int_{tc-\frac{T_{BM}}{2}}^{tc+\frac{T_{BM}}{2}} \beta \cdot sinc(K\tau_p(\tau - \frac{2r(t;r_0)}{c})) \cdot exp(j\frac{4\pi}{\lambda}(r_0))dt \tag{1.26}$$

Yet the problem is that this interpolation increases the computing time. Even so, this approach has no restriction with respect to the bandwidth or aperture size.

1.3 SAR Interferometry

With the intent to get more benefit form the SAR technology we combine two or more SAR images acquired at different conditions such as different times or/and different orbital positions. The phase difference between these images can provide extra information about the studied area. The earth height or the surface velocity can be inferred from the interferometric phase. The main configurations of SAR interferometry are the Across-Track and the Along-Track Interferometry.

On the other hand, there are two main acquisition modes. The first one is called *single-pass* and it is based on the acquisition at the same time of the images received by two antennas. The other mode is called *repeat-pass* and differs form the other because the images are taken at different instants. The *single-pass* mode gets good interferograms in terms of coherence but the baseline is restricted by the platform. On the contrary, in the *repeat-pass* mode there is no restriction in the baseline size anymore. However, it might suffer temporal and volumetric decorrelations between the different acquisitions in time.

1.3.1 Along-Track Interferometry

The Along-Track interferometry is used mostly for calculating the earth movement, the rivers and lakes flows, etc. It detects changes in a certain area between two different times. The basic structure of the interferometry mode consists of two antennas separated by a baseline B_{ATI} along the flight path (Fig. 1.8).

In this configuration, the received signals arrive in the receive channels.

$$\Delta_t = \frac{B_{ATI}}{v} \tag{1.27}$$

Where v is the velocity of the platform. If there are moving targets with a velocity V_R in the radial direction, there will be a phase ϕ_{int} between the acquisitions.

$$\phi_{int} = p \cdot \frac{2\pi}{\lambda} V_R \cdot \Delta_t \tag{1.28}$$

$V_R \cdot \Delta_t$ is the displacement where V_R is the velocity of the target. p refers to the antenna configuration. If both antennas transmit and receive p is 2 whereas when one antenna only receives p is 1.

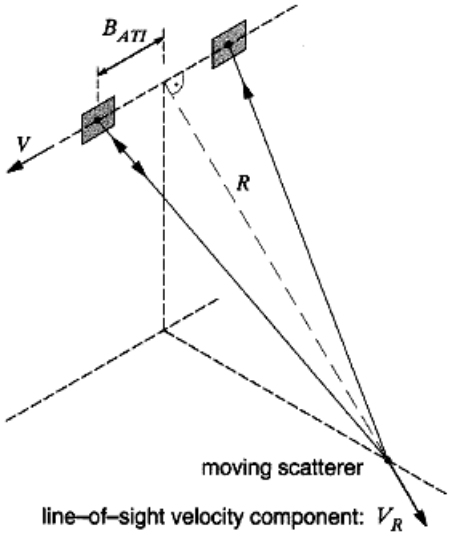

Figure 1.8: Along-Track Interferometry structure[8].

In the case that there is no displacement we receive the same information from both antennas and no range shift appears in the interferometric phase ϕ_{int}.

1.3.2 Across Track Interferometry

The Across-Track configuration is used for obtaining the DEM (Digital Elevation Model) of the earth surface. The system, which is presented in the Figure (Fig. 1.9) , has two antennas, the *master* and the *slave*. The antennas are separated by a baseline orthogonal to the azimuth direction with a tilt angle α .

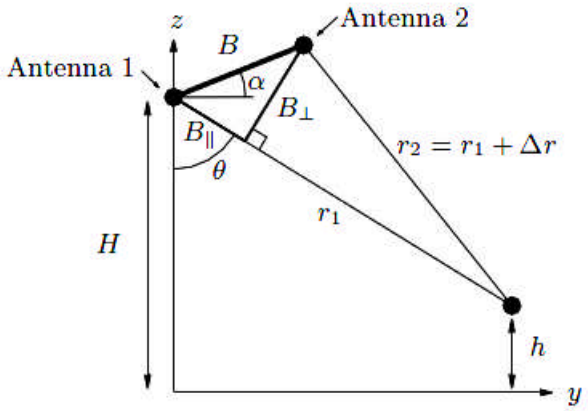

Figure 1.9: Across-Track Interferometry structure[9].

Firstly, we need to calculate the path difference Δ_r between the *master* and the *slave*. Af-

terwards, we compute the incidence angle θ. Assuming that the range distances between the antennas r_1 and r_2 are known, playing with the trigonometrical laws and doing approximations as in the Formula (1.32), where we assume that the range distances are much bigger than the baseline (*parallel-ray* approximation) [3], this angle can be estimated. Once the incidence angle is known, the height estimation is very simple (1.33).

$$\Delta_r = r_1 - r_2 \tag{1.29}$$

$$(\Delta_r + r_1)^2 = r_1^2 + B_2 - 2r_1 B \sin(\theta - \alpha) \tag{1.30}$$

$$\Delta_r = \sqrt{1 + (\frac{B}{r_1})^2 - \frac{2B}{r_1}\sin(\theta - \alpha) - 1} \tag{1.31}$$

$$\Delta_r \approx -B \cdot \sin(\theta - \alpha) \tag{1.32}$$

$$h = H - r_1 \cdot \cos(\theta) \tag{1.33}$$

In order to calculate the path distance between the antennas Δ_r, stereometric technics based on the amplitude of the images can be used. Although they are able to compute the path distance and, consequently, to provide a height estimation, these estimations are not usually as accurate as desired. Errors in the range distance measurement lead to errors in the height estimation around 100 times bigger. This is the reason why, to construct good DEM modes, we choose to use the interferometric information and the errors are reduced and smoothed. The use of the information given by the interferometric phase permits to have a accuracy in the order of a fraction of the wavelenght.

The interferogram is the multiplication of the complex image of the first image by the conjugate of the other (1.34). The interferometric phase of this multiplication is proportional to the path difference Δ_r between the *master* and the *slave* and, consequently, proportional to the incident angle θ (1.35).

$$I = I_1 \cdot I_2^* \tag{1.34}$$

$$\phi_{int} = -\frac{4\pi}{\lambda} \cdot \Delta_r \approx -\frac{4\pi}{\lambda} B sin(\theta - \alpha) \tag{1.35}$$

This interferometric phase is the difference between the phases of the images which has the following form for each of them

$$\phi_{slc} = -\frac{4\pi}{\lambda} r_o + \phi_{\sigma 0} \tag{1.36}$$

where $\phi_{\sigma 0}$ is the difference in the backscatters phases for the two acquisitions of the resolution cell. The backscattering coefficient of the interferometric images can be considered as equal in the *single-pass* mode.

It is important to remark that this interferometric phase is composed of to differentiated terms: one depending on the topography and the other, known as flat term, which is not related with the topography of the scene [3]. After some calculations and approximations the interferometric phase can be defined as follows

$$\phi_{int} = \phi_{ft} + \phi topo \approx -\frac{4\pi B \cos(\theta - \alpha)}{\lambda r \tan(\theta)}\delta_r - \frac{4\pi B \cos(\theta - \alpha)}{\lambda r \sin(\theta)}\delta_h \tag{1.37}$$

The term that appears multiplying δ_h is a matrix called k_z which will appear in the next chapters of the thesis as it is part of the data provided by the SAR systems, and gives the relation between the phase and the topography.

As it was said before, computing the path difference Δ_r using the interferometric phase really improves the accuracy of the DEM. The reason of this is that now the accuracy in the measurement of the Δ_r is proportional to the accuracy on the phase measurement.

$$\sigma_{\Delta_r} = \frac{\lambda}{4\pi}\sigma_{\Delta_\phi} \tag{1.38}$$

At this point, another problem appears as the interferometric phase is wrapped between $-\pi$ and $-\pi$. To turn this ambiguous phase into the unambiguous phase, which is the appropriate one for the height estimation, we need an unwrapping process. This unwrapping process is the main topic of the thesis and is explained in more detail in the next chapters. This unwrapping process also needs to be complemented by and absolute calibration of the phase if we want to be precise.

Because of this wrapping phenomenon, it is important to keep in mind the concept of height of ambiguity $h_{2\pi}$, which is the height jump corresponding to a phase change of 2π.

$$HoA = h_{2\pi} = \frac{\lambda r \sin(\theta)}{2B \cos(\theta - \alpha)} \tag{1.39}$$

Both in this height ambiguity equation (1.39) and in the equation (1.35), we observe that big baselines are preferable as they increase the accuracy of the systems. High frequencies have the same property. Nevertheless, if the baseline is too large, the baseline decorrelation will produce such a big noise that the system performance is deteriorated.

As the quality of the height estimation depends on the interferometric phase measurement, it is necessary to examine how trustful this measure is. That is the reason why we observe the interferometic coherence

$$\gamma_{coh} = \frac{|E[I_1 I_2^*]|}{\sqrt{E[|I_1|^2]E[|I_2|^2]}} \tag{1.40}$$

This coherence varies from 0 to 1. The values near to 0 correspond to noisy images and the values near to 1 correspond to good quality information. In the equation $E[]$ is the expectation operator and, taking into account the ergodicity, it can be calculated using a spatial average. Usually in this average, the computed pixels are the neighbors of each pixel and the number of these averaged pixels is called number of looks.

Moreover, the coherence is the result of the multiplication of different decorrelations [3]:

- Baseline or geometrical decorrelation
- Doppler centroid decorrelation
- Volume decorrelation
- Thermal noise decorrelation
- Temporal decorrelation
- Processing decorrelation

While the temporal and the volume decorrelations cannot be improved, the other can be optimized with the use of different filters and processing algorithms.

On the other hand, the coherence is an estimation and therefore, it is biased. The estimation tends to overestimate the low coherence [2] and hence special care should be taken with the coherence in the difficult parts of the interferogram. The bias can be faced with a big number of looks. With large number of independent samples the coherence becomes asymptotically unbiased. In Fig. 1.10 we can see how the coherence approaches to the *Cramer Rao bound* coherence as the number of samples is bigger.

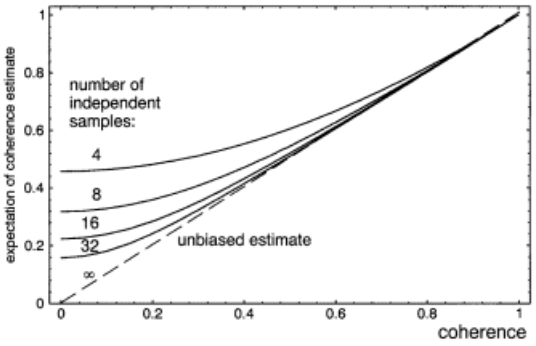

Figure 1.10: Coherence bias depending on the number of looks[10]. .

1.3.3 E-SAR and F-SAR airbones systems

E-SAR(Experimental SAR)is an experimental airbone Synthetic Aperture Radar system conceived by the DLR Microwaves and Radars Institute. Nowadays, it is obsolete. The first images delivered by the E-SAR were obtained in 1988. Since then, the quality of these images and the system configuration have been constantly upgraded. The airbone platform carrying the SAR system is the D*O*228-212, a STOL (Short Take-off and Landing aricaft). It operates

about 6000 m above the sea level with a ground speed of 90 m/s and it can work during 2.5 and 4 hours.

Figure 1.11: E-SAR aircraft[11]. DO228-212 airbone with the E-SAR itself on board.

Concerning the radar itself, it operates simultaneously in four frequency bands (X,C,L and P), which means that the wavelength range goes from 85 to 3 cm. The polarization of the signal can be horizontal or vertical, and even it can be switched in each pulse (*polarimetric*) with this sequence HH-HV-VV-VH [6]. Both single-pass and repeat-pass modes can be implemented by E-SAR and can be combined with polarimteric.

To carry out a calibration in the final DEM, there are spread around the DLR airfield in Oberpfaffenhofen different radar corner reflectors.

In the last decades, E-SAR has been used for different experimental and measurement campaigns in Europe principally. Nevertheless, as a consequence on the increasing demand of data simultaneously acquired at different wavelengths and polarizations, as well as an improvement in the resolution, the successor of the E-SAR, the **F-SAR**, was conceived and its maiden flight took part in 2006.

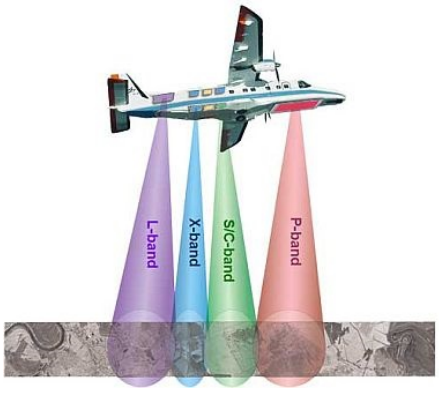

Figure 1.12: F-SAR aircraft[12]. F-SAR acquires data simultaneously in different bands.

The most interesting capacities of F-SAR is that is a full modular system in the X, C, S, L and P frequency bands. Now the system works also in the S-BAND. Furthermore, it has full polarimetric capability in all frequencies. The most interesting feature for this thesis is the

single-pass and repeat-pass simultaneous interferometric capability in the X-BAND and in the S-BAND (the measures used for this thesis come from this characteristic).

Concerning th platform where the F-SAR system setted, it is the same as the E-SAR, the DO228-212 airbone. However, another options are being considered with the goal of improving the performance in terms of flight range and altitude.

More information and the technical specification can be found in the DLR web [6] and [7].

2 State of the art

2.1 Phase unwrapping problem

As it was introduced in the Interferometry SAR presentation, the extra information used for the construction of the Digital Elevation Modes (DEM), is the interferometric phase.

This interferometric phase corresponds to the phase of the multiplication of one of the complex images of the interferogram with the complex of the other and is just the difference between the phase of each image.

$$I(i,j) = I_1(i,j) \cdot I_2(i,j)^* = |I_1||I_2|exp(j\psi(i,j)) \tag{2.1}$$

$i = 1, ..., M$, $j = 1, ..., N$ and MXN is the size of the interferogram.

But this phase is *wrapped*, which means that it has a value between $-\pi$ and π and differs from the absolute phase in every pixel by a multiple of 2π. Only the absolute phase has a direct relation with the topography.

$$\phi(i,j) = kz(i,j) \cdot h(i,j) \tag{2.2}$$

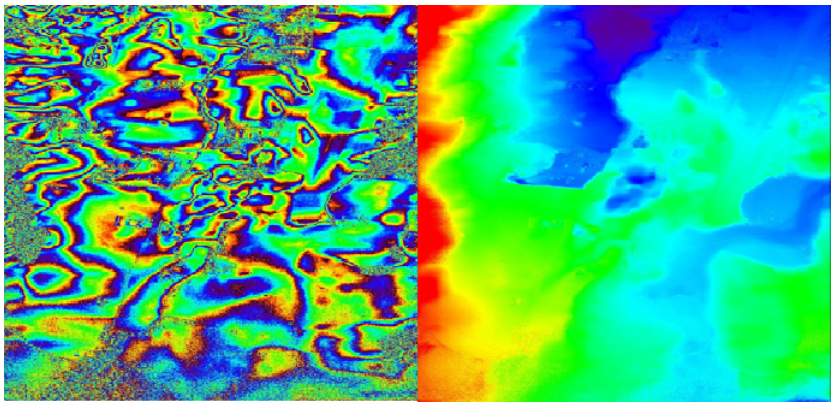

Figure 2.1: Unwrapping example[1]. Wrapped phase at right, and unwrapped phase at left of a scene studied in Kaufburen (Germany). Data acquired by the F-SAR system.

Given that, the problem to be solved is to transform this *ambiguous* phase ψ into an *unambiguouos* phase ϕ.

$$\phi(i,j) = \psi(i,j) + 2\pi n_{cycle}, n_{cycle} \in \mathbb{Z} \tag{2.3}$$

Under the assumption that the unwrapped phase gradients in the adjacent pixels (the difference between them) are equivalent to the wrapped phase gradients, and taking into account that these last gradients $\in [-\pi,\pi]$ (this condition is known as *Itoh condition*) the unwrapping problem is easily solved. The unwrapped phase could be computed by integrating the wrapped gradients pixel to pixel along and arbitrary path. However, this assumption is quite pretentious because in the majority of the interferograms we have to cope with gradients bigger than π which can be named *discontinuities*. The origin of these discontinuities is varied and helps us to differentiate the different unwrapping problems and challenges.

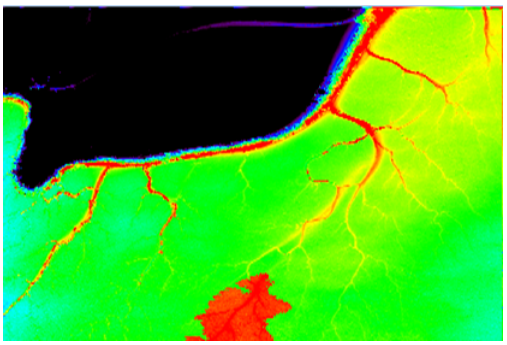

Figure 2.2: Unwrapped river[2]. Error in the unwrapping process in an area with a river with multiple meanders.

We can assure that the *repeat-pass* mode leads to more problems in the unwrapping process. Nevertheless, if the unwrapping in performed correctly, the quality of the DEM obtained is better that the one obtained with the *single-pass* mode, due to the dependence of the height sensitivity with the inverse of the baseline.

Concerning the main unwrapping problems, on the one hand there are discontinuities caused by the interferometric decorrelation. In noisy areas with low coherence there can be some discontinuities as a consequence of the lack of *knowledge* on this area. Thus, we have *aliasing* errors caused by the presence of phase noise. The more problematic areas are noisy areas with low backscattering like forests. Water areas like rivers, lakes or coasts, which can be classified as low-coherence zones, are also complicated. In the image above (Fig. 2.2) we can see how a river with its branches and meanders is erroneously unwrapped. On the left bank of the river, the solution should have a similar value to the right bank, which is not the case. These errors can be reduced using a large multilooking (averaging) before the unwrapping, but this implies a resolution loss.

On the other hand, we can find discontinuities in steep regions with high sloped mountainous areas. In this kind of areas there are big jumps in height between neighbors pixels which exceed the height of ambiguity, height that was presented in the introduction but that should be recalled again (2.4). There is an undersampling phenomenon due to locally high fringe rates.

$$HoA = h_{2\pi} = \frac{\lambda r \sin(\theta)}{2B\cos(\theta - \alpha)} \tag{2.4}$$

We repeat that big baselines and high frequencies improve the accuracy of the systems. However, the size of the baseline has some limits because this increase in size involves baseline decorrelation that can be harmful for the unwrapping process. We can see some unwrapping errors in the unwrapped interferogram of a rugged terrain in Sardegna (Italy) in the following image (Fig. 2.3).

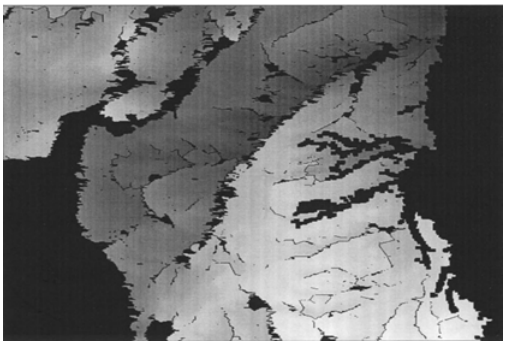

Figure 2.3: Steep area[3].Unwrapped rugged terrain in Sardegna.

As we want to reduce the phase fringes so as to face an easier unwrapping, the flat term (1.37) uninfluenced by the topography characteristics is subtracted.

Finally, it can be pointed another problem. With respect to the computing time, it is obvious that the bigger the interferogram, the heaviest is the computing time. As a result, at some point the algorithm is unworkable in time and some solution should be taken. One solution can be to divide the interferogram in a mosaic formed by small tiles [8]. Unwrapping each tile separately and in parallel will significantly reduce the execution time. This leads to boundary problems in the global solution assembling. Anyway, assembling optimization models can help to overcome the setback.

An important thing that should not be overlooked is the phase *calibration*. As a consequence of different imperfections and lack of precision in different measures

- Measurement of the baseline
- Measurements of the angles
- Measurement of the platform position
- Measurement of the range delay

Is is interesting to underline the differences between the *single-pass* and the *repeat-pass* when it comes to these kind of errors. In the *single-pass* mode the geometrical decorrelation is not important and the temporal decorrelation doesn't exist. On the contrary, in the *repeat-pass* mode both exists and are important. Hence, the calibration first in the *single-pass* phase acquisition could be helpful for the calibration of the *repeat-pass* acquisition.

Another reason for this calibration is that there is an offset in the image an we are in the dark about it because it should be a multiple of 2π but in the reality it is not. One solution for all these errors can be given by *sensitivity equations* [3]. The idea is to derive the interferometric height reconstruction equation for the different parameters needed to determine the components of this equation, which are those listed above. This method con be improved by putting different reflectors in different positions around the area. The position of these reflectors are obviously known and therefore a linear systems of equations facilitates the calibration.

$$\mathbf{T} = \mathbf{P} + r\mathbf{l} \tag{2.5}$$

This is the scatter position vector $\mathbf{T}$ in function of the position of the platform vector $\mathbf{P}$ and the range target distance r. $\mathbf{l}$ is an unitary vector. This is the function which is going to be derived with respect to the different paramenters.

More obvious is the solution of using an external DEM (Digital Elevation Mode) to compare and hence to calibrate. This approach is suitable to correct the offset. Azimuth and range inaccuracies can also be improved.

That being said, many accuracy errors should and could be solved during the phase unwrapping itself and not afterwards. As it is known, in the *repeat-pass* SAR interferometry mode, there are inconsistencies in the position of the antennas, which means azimuth-dependent baseline errors known as *residual motion* errors. If the co-registration error along azimuth is integrated, the residual motion errors can be estimated and thus a phase correction can be made. Then, many errors don't need to be remedied in a latter process.

2.2 Phase unwrapping methods

There are several existing unwrapping phase algorithms and they can be classified globally in four groups [9]:

- Minimum L^p
- Path following algorithms
- Bayesian/regularization
- Parametric model

The methods cataloged as Minimum L^p norms rely on the minimization of the L^p [10] difference between the absolute phase differences and the wrapped phase differences. They are *global* in the sense that to obtain a solution a minimization in all the observed phases is carried out. The best minimization corresponds to the case when p is 0, because it does not smooth the discontinuities and hence generates the most accurate solutions. Nevertheless, the minimization of L^0 norma is a $NP-hard$ problem and some approximate optimizations are needed. As p grows the minimization tends to smooth the discontinuities but the computing of the process is more feasible and simple. One interesting case is L^2 and it is called *least-squares method* [11].

The path following algorithms are those which follow a line iteration scheme over the wrapped phase received. These algorithms consider that the difference between the adjacent pixels in iteration lines is less than π, what means that the *Itoh* condition is fulfilled. Whenever a difference between neighbors is bigger than π, an error appears. As a consequence, later optimizations for solving these errors such *branch cuts* [12] and *quality maps* [13] are used. One algorithm belonging to this group and on which is based the half of this thesis is the Region Growing algorithm. In the subsection 2.3.3 it is broadly presented.

The third group corresponds to the Bayesian/regularization methods . These methods use not only the wrapped phase, but also complementary information like the coherence, the correlation or the *kz* provided by the backscattered echoes received by the SAR. This information gives an *a priori* knowledge that can be helpful for the statistical methods and it is directly provided by the InSAR images. A lot of unwrapping methods benefit from the *a priori* knowledge. Specially, the second part of the thesis works with algorithms mostly inspired in this approach.

There is finally the parametric algorithms. As the name implies, this methods constraint the unwrapped phase to a parametric surface. To characterize the surface, polynomials of different order could be used. Obviously, the higher the order, the more accurate unwrapping is achieved, but on the contrary, the unwrapping implementation gets more complicated. There are some cases that it may be opportune to divide the interferogram in different parts, where a viable polynomial is used to describe each interferogram part. A very good model of this is the Local Planes Parameters Estimation (LPPE), fully explained in 2.4.1.

2.3 STEP algorithms

STEP is a project that has its origin in the idea of creating a highly modular and generic airbone SAR processor. All the data coming from the F-SAR aircraft are transformed into the internal formats of the STEP project for the subsequent storage and processing. The goal is to draw up a big reference where all the necessary for the INSAR (in this case the F-SAR) data treatment and complementary necessities could be found. STEP is organized in different sections to supply the project with the proper structure:

- **algorithms**: of general use
- **fsar**: more specific routines
- **gui**: graphical interface routines
- **io**: reading and writing routines
- **step**: STEP processing routines
- **tools**: additional tools to the normal processing
- **oldstuff**: obsolete routines that could be helpful

As far as this thesis is concerned, in the STEP programming resources, there are coded three important phase unwrapping algorithms:

- PUMA
- SNAPHU
- Region-Growing

The three algorithms are presented in the next pages and, in order to compare them, some tests in a simulated profile have been done. These tests are commented in the next chapter "Developed algorithms and experiments".

2.3.1 PUMA: Phase unwrapping max-flow/min-cut

The PUMA (Phase Unwrapping Maz Flow), whose information can be found in [9] is just an energy minimization for phase unwrapping where the energy minimization is carried out by a sequence of max-flow/min-cut calculations

The minimization is applied to Markov fields. We define *clique* as a set of adjacent pixels and we classify the potentials of these cliques as convex or nonconvex. This classification determines the employed optimization process.

In the case the clique potentials are convex, the minimization algorithm relies in a sequence of binary minimizations which are resolved by a max-flow/ min-cut calculation on a given graph. There we have the origin of the algorithm name. Therefore, for this case of convex potentials, the PUMA is a generalization of the classical minimum L^p norm problem that works with more classes of energies [9]. The next formula(2.6) must to be fulfilled by the potential $V(\cdot)$ if it is convex.

$$V(a) + V(c) - V(b) \geq V(a + c - b) \tag{2.6}$$

We can cite as examples of potentials that meet this criteria the clique potential of the classical L^p norm $V(\delta\phi) = |\delta\phi - W(\psi)|^p$ (with $p \geq 1$ and W the wrapping operator) or convex potentials like the quadratic clique potential $V(x) = x^2$.

On the other hand, unknown discontinuities between neighbors produce nonconvex clique potentials and the minimization problem is then a NP-hard one. As a consequence. the individual binary minimization complemented by the max-flow/min-cut calculation cannot be applied anymore. Hence another algorithm should be applied in these cases. This complementary algorithm is based first of all in an enlargement of the configuration space. Now, sometimes jumps bigger than 1 (no more binary) are needed. Secondly, the complementary algorithm is also based in the application of majorize-minimize (MM) concepts to the energy functions when there are *non regular* pair of pixels [9]. Though the algorithm is different in this nonconvex case, the general phase unwrapping approach for convex and nonconvex potentials is called PUMA simply for simplicity in the nomenclature.

The image (Fig. 2.4) represents a *clique*, a pixel whith its direct neighbors. The vs and hs represents the discontinuities (0 discontinuity,1 no discontinuity) and come from quality maps, which can be computed out of the InSAR correlation maps. These maps are usually noisy and the discontinuities cannot be see with clarity, determining the use of nonconvex or convex potentials.

The energy which has to be minimized is

$$E(k^n + \delta|\psi) = \sum_{ij \in G_0} V(\Delta\phi^h_{ij}) v_{ij} + V(\Delta\phi^v_{ij}) h_{ij} \tag{2.7}$$

$$\Delta\phi^h_{ij} = [2\pi(k_{ij} - k_{ij-1}) - \Delta\psi^h_{ij}] \tag{2.8}$$

$$\Delta\phi^v_{ij} = [2\pi(k_{ij} - k_{i-1j}) - \Delta\psi^v_{ij}] \tag{2.9}$$

$$\Delta\psi^h_{ij} = \psi_{ij-1} - \psi_{ij} \tag{2.10}$$

$$\Delta\psi^v_{ij} = \psi_{i-1j} - \psi_{ij} \tag{2.11}$$

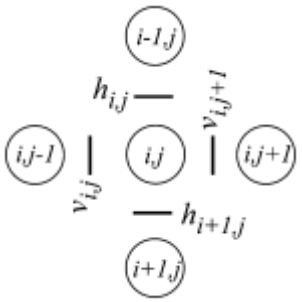

Figure 2.4: PUMA clique[4]. Example of *clique*: a pixel surrounded by its neighbors and the values of the *quality maps*.

where k is the 2π multiple which is going to unwrap the wrapped phase ψ_{ij}. In short, the intention is to obtain the k value that minimizes this function.

In the case of having convex clique potentials, binary optimizations of this energy are developed with the next structure

$do\ k^{n+1} = argmin\ E(k^n + \delta|\psi)$

$while\ E(^{n+1}|\psi) < E(k|\psi)$

where n is the number of iterations that assure the reaching of the minimum. If we introduce $k^{n+1}_{ij} = k^n_{ij} + \delta_{ij}$ in the formulas (2.8) and (2.9) and with a bit of manipulation we get a new presentation of the energy function prepared for the mapping of the binary optimization onto max-flow problems.

$$\Delta\phi^h_{ij} = [2\pi(\delta_{ij} - \delta_{ij-1}) + a^h] \tag{2.12}$$

$$\Delta\phi^v_{ij} = [2\pi(\delta_{ij} - \delta_{i-1j}) + a^v] \tag{2.13}$$

$$E(k^n+\delta|\psi) = \sum_{ij\in G_0} V[2\pi(\delta_{ij} - \delta_{ij-1}) + a^h]v_{ij} + V[2\pi(\delta_{ij} - \delta_{i-1j}) + a^v]h_{ij} = \sum_{ij\in G_0} E^{ij}(\delta_i, \delta_j) \quad (2.14)$$

The binary problem can be represented by a graph with υ nodes and ε edges. The edges are responsible for the nodes connection. We have to count as nodes, apart from the pixels, two more, the source s and the sink t. s and t are the terminals and can be seen as the set of labels that can be assigned to the pixels. If we simplify a_h and a_v to a, and h_{ij} and v_{ij} to d_{ij}, we get

$$E^{ij}(0,0) = V(a)d_{ij}; E^{ij}(1,1) = V(a)d_{ij}; E^{ij}(0,1) = V(-2\pi + a)d_{ij}; E^{ij}(1,0) = V(2\pi + a)d_{ij} \quad (2.15)$$

If the pair of pixels are *regular* ($E(0,0)$-$E(1,1)$>$E(0,1)$-$E(1,0)$), the binary optimization is graph representable. The global graph of the problem is the union of elementary graphs of each pair of neighbors. The elementary graphs consist of four nodes s,t,v,v', where v and v' refer to the pixels, and these nodes are joined between them by edges depending on the values of the energy terms defined above (2.15). In the figure we have an example taken from [9] where $E(1,0)$-$E(0,0)$>0 and $E(1,0)$-$E(1,1)$>0 and, for this reason, it has the edges in this sense. If this inequalities weren't true, we would have the diagram in the other way around. At right of the elementary graph, there is the global picture of the problem.

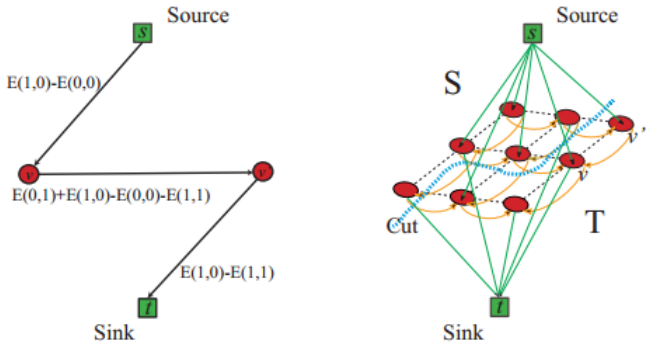

Figure 2.5: PUMA graph[5]. Elementary graph at left, global graph at right.

Once the energy terms are calculated for every vertical and horizontal pixel and the graph is constructed, the minimum is found straightforward by the binary optimizations following each one the max-flow/min-cut calculation [14] on the graph. A s/t graph cut on the graph is a partition of the graph in two disjoint subsets S and T (s is in S, t is in T). The cost of this graph is the sum of the boundary edges. Therefore, the minimum cut on a graph is the cut which involves a minimum cost. And this minimum cut corresponds to the *maximum flow* from the source s to the sink t. In this way, if the edge weights are based on parameters of energy, the *min-cut/max-flow* leads to a minimum value of this energy.

The procedure of PUMA in the case of nonconvex potentials is well presented in [9]. This document has also more detailed information about the complexity of the optimization problems and the different classes of clique potentials. Nevertheless, the topic is too deep for this thesis where the PUMA algorithm has only be tested to be compared with the truly studied methods in the thesis.

2.3.2 SNAPHU

SNAPHU is also one of the unwrapping existing unwrapping algorithms implemented by STEP. It is an implementation of a Statistical-cost, Network-flow Algorithm for Phase Unwrapping (SNAPHU) proposed by Chen and Zebker [8]. Posing the problem of phase unwrapping with a network model [15], it is necessary to differentiate among the different phase unwrapping solutions. For this purpose, we rely on the use of objective functions that map the possible unwrapped solutions to scalar costs [8]. In the particular case of SNAPHU, it uses the following objective function

$$minimize \sum_{k} g_k(\Delta\phi_k, \Delta\psi_k) \tag{2.16}$$

where ϕ_k is the individual unwrapped phase gradient and ψ_k individual wrapped one. In the network model, the phase difference between pixels determine the arcs joining the pixels, and hence the *flow* vectors in these arcs correspond to the difference in cycles between ϕ_k and ψ_k. In order to turn the arc's flow $(\phi_k - \psi_k/2\pi)$ into a scalar cost, the function g (2.17) is used. k guarantees this scalar cost calculation in all the columns and rows of the network. To achieve this minimization, a maximum a posteriori (MAP) estimation is employed. Consequently, the g cost functions are simply based on the unwrapped-gradient probability density functions

$$g_k(\Delta\phi_k, \Delta\psi_k) = -log(f(\Delta\phi_k|\Delta\psi_k, I, p)) \tag{2.17}$$

where I is the intensity and p the interferometric correlation, which means that the cost functions vary according to local variables. So the goal is to minimize the cost functions looking for obtaining the unwrapped phase with the biggest probabilty. Nevertheless, this task is not so easy because this complex and changing statistical cost functions turns the problem into a nonconvex optimization problem. In fact, it constitutes a $NP\text{-}hard$ problem. The solution for this setback, after considering some approximations, are nonlinear network-flow techniques [16]. Starting from an initial and feasible solution, SNAPHU makes iterative incremental flows in the different arcs and in the different directions trying to find solutions with smaller cost [17]. When in the iterations directed cycles that have net negative incremental costs are found, the algorithm increases the flows in that path directions. This is how SNAPHU tries to pass from different feasible solutions until it finds the optimal solution, with the minimal cost. As we have said, the network-flow optimization is a $NP\text{-}hard$ problem and sometimes the optimal solution is not assured. This the case for instance of

interferograms with big sizes, where maybe it is convenient to divide the image in tilts and apply SNAPHU in each tilt in parallel as it is proposed in [8].

SNAPHU always produces complete unwrapped solutions, and it normally does not generate phase errors bigger than 2pi. However, it produces some noisy trends, smaller than π, which are more difficult to identify.

One interesting note about SNAPHU is that it incorporates three built statistical methods as the statistics provided by the input data depend on the kind of data [17]. Therefore, we have a model for topographic data, for deformation data and for smooth generic data.

2.3.3 Region Growing Algorithm

The Region-Growing algorithm is one of the different existing algorithms for INSAR phase unwrapping and is fully explained in [18]. The strength of this algorithm is its utility in noisy interferograms. It is possible to unwrap low coherence regions with a low probability of error. Another advantage is that it allows changes between two adjacent pixels bigger than π radians which is ideal to deal with steep topography. That means that it works in areas where the Itoh condition is not satisfied.

This method starts in different growing regions with the smoothest topography. The regions are born in pixels called *seeds* where the unwrapping confidence is high which means that the phase is smooth and does not change too much between neighbor pixels. These regions grow along dynamics paths where the data quality is high.

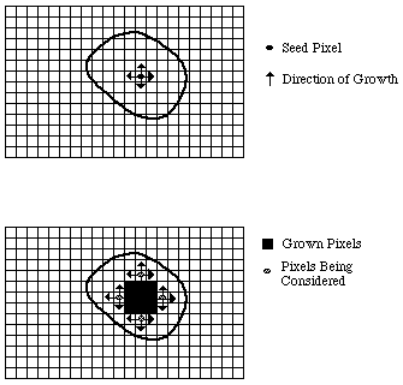

Figure 2.6: Region Growing[6]. Seed pixel and growing direction in the first square and grown pixels with the new considered ones in the second square.

In the Region Growing algorithm, the unwrapping of each pixel is made out of slope predictions made from its unwrapped neighbors (2.18). As it was said before, the use of these predictions permit to produce differences between pixels larger than π. Information from different directions is used in this procedure and helps to reduce the possible error of certain pixels. A weighted prediction ϕ^p is used in which the weights w_k vary according to

the proximity to the pixel being unwrapped. The prediction in each direction can be constant (2.19) or linear (2.20) depending to the number of pixels already unwrapped in the different lines or paths.

$$\phi^p = (\sum_{k=1}^{N_u} w_k \phi_k^p)/(\sum_{k=1}^{N_u} w_k) \tag{2.18}$$

$$\phi_k^p = \phi[k] \tag{2.19}$$

$$\phi_k^p = 2\phi[k] - \phi[k'] \tag{2.20}$$

Once we have the predictions, the unwrapping is simply completed in this way calculating an ambiguity number m. However, as it is explained in the next paragraph, the unwrapping attempt could be accepted or rejected.

$$m = nint(\frac{\phi^p - \phi_w}{2\pi}) \tag{2.21}$$

$$\phi_u = \phi_w + 2\pi m \tag{2.22}$$

ϕ_u refers to the unwrapped phase and ϕ_w to the wrapped phase.

Each unwrapping attempt is checked to see if it is reliable. There can be made different kinds of measures like the average deviation of the individual predictions (2.23), the difference between the unwrapping result and the composite prediction (2.24) or the local coherence (2.25). The subscripts m and s in the coherence formula refer to the *master* and *slave* images. These measures are compared with a maximum or minimum threshold and they can be combined creating different reliability tests. The threshold is gradually relaxed in order to follow a high to low reliability path. We can apply the same threshold to the first two equations and then relaxing it or set this common threshold constant and play with the coherence [18]. In particular, in this thesis a measure of the local coherence of the interferogram is used. This coherence should be bigger than a threshold that is progressively reduced from a value close to 1 (0.85) to a value close to 0 (0.15).

$$d_p = (\sum_{k=1}^{N_u} w_k |\phi_k^p - \phi^p|)/(\sum_{k=1}^{N_u} w_k) \tag{2.23}$$

$$d_u = |\phi_u - \phi^p| \tag{2.24}$$

$$e = |Ea_m e^{j\phi_m} a_s e^{-j\phi_s}|/\sqrt{Ea_m^2 Ea_s^2} \tag{2.25}$$

The regions are classified with an arbitrary number but following an order so that the regions originated from more coherent seeds have lower numbers. Every pixel has a record

of the regions where it has been unwrapped and the value of the ambiguity number m in each region. There are two stages in the growing process. A *growing* stage when the regions are growing and the *relaxing* stage when the thresholds are relaxed as a consequence of unwrapping failures.

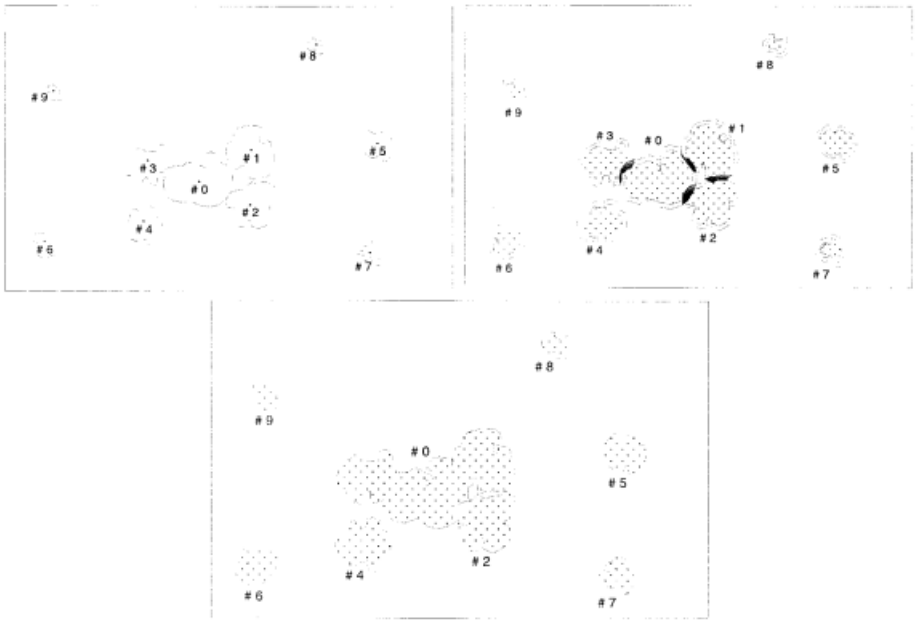

Figure 2.7: Merging regions[7]. Image taken from [18] showing the growing and merging process.

At some point the growing regions meet and an overlap area appears. The algorithm tries to merge the converging regions. In every pixel the difference between the ambiguity numbers m , is compared with an estimation. In the case the majority of the pixels N_c, according to an established threshold t_r, satisfies this estimation both regions are merged (2.26). The region with the highest *classification* number takes the one of the other region and each pixel takes as definitive ambiguity number the one of "good" region. However, all the pixels that not fulfill this requirements don't take part of this union and should be unwrapped again later by a new growing region. That means that new growing regions could appear in these *gaps* product of the merging process. In the complementary case the threshold is not achieved, the fusion is not carried out and the overlap area is reset.

$$N_c \geq t_r \tag{2.26}$$

N_c is the number of pixels that agree with the estimation and t_r is the threshold.

In conclusion, this unwrapping algorithm is quite good when the interferogram to be unwrapped correspond to an extreme topography area. It is due to the diversity of paths, the different directions examined in the process and the possibility of having differences between adjacent pixels bigger than π. There are more possibilities to make up for the errors

with this procedure. The computing time employed for this is going to be important. Nevertheless, this time is bigger in other STEP algorithms. For this and more reasons, it has been the algorithm chosen for developing the dual frequency approach.

2.4 Statistical Multichannel Phase Unwrapping (MCPU) Methods

These methods rely on the maximization of the multichannel likelihood function of the interferometric phase after combining two or more independent interferograms. This estimation can be afterwards complemented by different methods such as the Local Planes Parameters Estimation (LPPE) or the use of an inhomogeneous Gaussian Markov Random Field (GMRF) to compute an a priori model. Moreover, both complements are not mutually exclusive. These methods have the advantage that the height is directly calculated without the necessity of any additional filtering. This is an important consideration. As the name indicates, the algorithms use the information provided by N channels of an image of size M. Hence, for the phase unwrapping and the height reconstruction these methods dispose of NxM wrapped phases $\phi_n(i,j)$. (i,j) indicates the position of the pixel in the image of M pixels, and the term n refers to one of the N channels. The term 'multichannel' can refer to multi-frequency or to multi-baseline, so this approach can be made in two ways. Nevertheless, the multi-baseline way is less precise as we already discussed. Its main problem is that the single-channel likelihood functions must be expressed with precision and in the multi-baseline case this is quite difficult to achieve with the accuracy of the inertial navigation systems [19]. For this reason, this thesis focuses on the multi-frequency approach.

Once the single-frequency likelihood functions are determined (2.28), they are combined to form the Multichannel Likelihood function (2.27). This ML promotes the achievement of a global maximum [19]. Whereas in the single frequency *pdf* infinite solutions can be obtained, with the MF approach we get only one (Fig. 2.28). Actually, under certain conditions, even with two frequencies we could avoid the multiple solution and ensuring the uniqueness value of h [20]. For this the ratio between f_1 and f_2 should not be rational, and then the joint likelihood function is not periodic.

$$F_{mf}(\Phi|h) = \prod_{n=1}^{N} f(\phi_n) \tag{2.27}$$

$$f(\phi_n|h) = \frac{1}{2\pi}\frac{1-|\gamma_n|^2}{1-|\gamma_n|^2\cos(\phi_n - d\frac{4\pi}{\lambda_n}h)}(1+\frac{|\gamma_n|\cos(\phi_n - d\frac{4\pi}{\lambda_n}h)\cos(-|\gamma_n\cos(\phi_n - d\frac{4\pi}{\lambda_n}h)^{-1})}{(1-|\gamma_n|^2\cos(\phi_n - d\frac{4\pi}{\lambda_n}h)^{1/2})}) \tag{2.28}$$

Note that for simpler operation, the phase is now only ϕ_n, with n the number of different phase acquisitions or channels. γ is the coherence

Although the different channels are considered independent, this is not absolutely true because in the INSAR acquisition some noise and interferences between the channels are

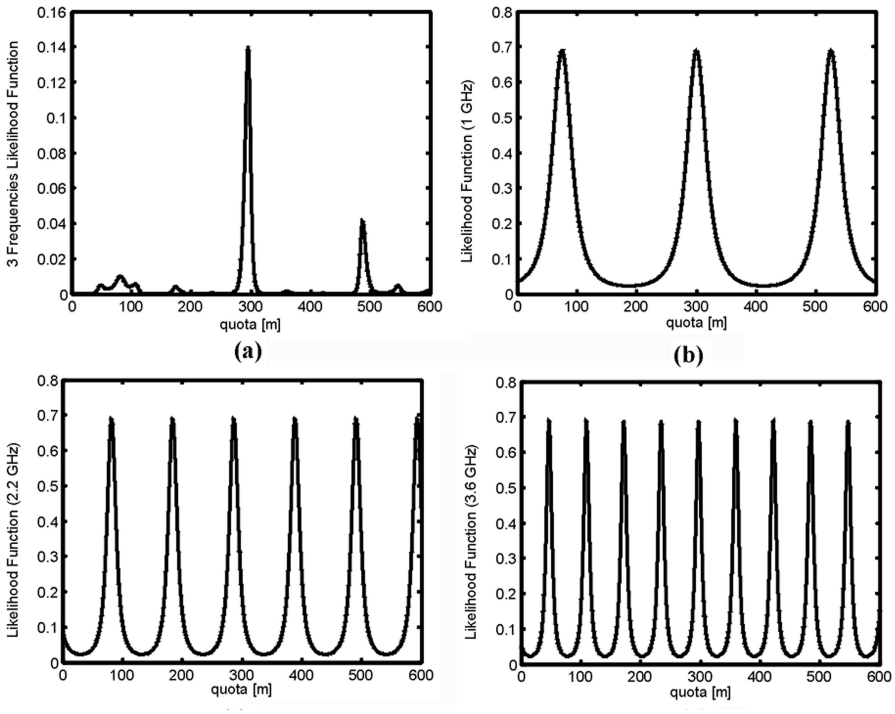

Figure 2.8: Multichannel Likelihood Funtion example[8]. In [19] we can see the multichannel likelihood function resulting from the combination of three different frequencies: 1, 2.2 and 3.6 GHz (no rational ratio between them.)

produced. Anyway, this "dependency" between channels can be ignored still obtaining reliable results. Making use of this multichannel likelihood function the height estimation in each pixel is straightforward.

$$\hat{h} = arg \max_{h} F(\Phi|h) \tag{2.29}$$

Φ is the wrapped phase in this case. If we want to develope and *a priori* multichannel MAP estimation we have to complement (2.29). In order to achieve this, wecan use a GMRF to model h.

$$\hat{h} = arg \max_{h} F(\Phi|h) g_{\beta}(h) \tag{2.30}$$

This point will be discussed in the section 2.4.2.

2.4.1 MCPU through Maximum Likelihood Estimation of Local Planes Parameters

In the general ML (Maximum Likelihood) MCPU algorithm explained above the estimation in each pixel depends just on this specific pixel. In order to achieve a better estimation, the

information of the neighbors could be used in some way to strengthen the unwrapping process. This is important in systems which have some weaknesses. This additional information provided by the bordering pixels could represent a great support.

In the height estimation of one pixel we count on the help of N independent measures of the wrapped phase in this pixel. Now, N_c more independent measures are combined with the previous ones. An area surrounding the considered pixel which can be named *cluster* N_{ij} provides these data. This N_c measures correspond to the wrapped phase of the pixel and its $N_c - 1$ adjoining pixels for each one of the N measures. The combination of these measures makes NxN_c independent measures of the wrapped phase. The height surface of the cluster can be approximated by a plane.

$$z(p,q) = a(i,j)p + b(i,j)q + c(i,j), (p,q) \in N_{ij} \tag{2.31}$$

The only plane not considered is the perfect vertical one. p and q are the range and the azimuth steps.

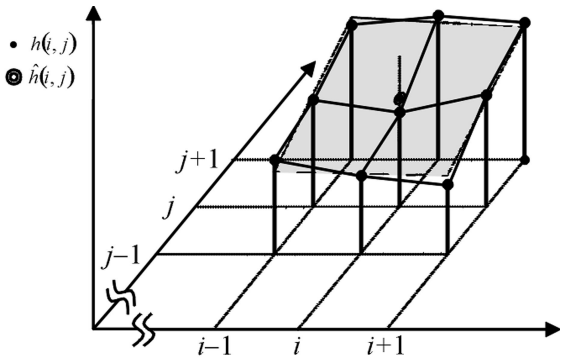

Figure 2.9: Local plane[9]. Local plane example for the position (i,j) considering a cluster N_{ij} of nine pixels.

The change consists in not processing each pixel independently from the others and looking for the best a, b and c parameters of the most approximated plane (of the *cluster* area), in the ML (Maximum Likelihood) sense (2.34), to the good height estimation of the pixel. These directional parameters are now the unknown parameters ($x_{i,j} = [a(i,j)b(i,j)c(i,j)]^T$). This estimation is referred as the Local Planes Parameters Estimation (LPPE) [19].

$$f(\phi_n(p,q)|x_{ij}) = \frac{1}{2\pi}\frac{1-|\gamma_n|^2}{1-|\gamma_n|^2\cos(\phi_n(p,q) - d\frac{4\pi}{\lambda_n}(ap+bq+c))} \cdot (1+K) \tag{2.32}$$

$$K = \frac{|\gamma_n|\cos(\phi_n(p,q) - d\frac{4\pi}{\lambda_n}(ap+bq+c))\cos(-|\gamma_n\cos(\phi_n(p,q) - d\frac{4\pi}{\lambda_n}(ap+bq+c))^{-1})}{(1-|\gamma_n|^2\cos(\phi_n(p,q) - d\frac{4\pi}{\lambda_n}(ap+bq+c))^{1/2})} \tag{2.33}$$

$$\hat{x}_{i,j} = argmax \prod_{(p,q)\in N_{ij}} F_{mf}(\Phi(p,q)|x_{i,j}) = \prod_{(p,q)\in N_{ij}} \prod_{n=1}^{N} f(\Phi(p,q)|x_{i,j}) \tag{2.34}$$

For a robust search of the maximum, an optimization algorithm like *simulated annealing*, which avoids getting stuck in a local minimum, can be used. This algorithm is presented in the Appendix 1. Finally, the height estimation is the value of the considered point (i, j), center of the cluster N_{ij}, in the found plane.

$$\hat{h}(i,j) = \hat{a}(i,j)i + \hat{b}(i,j)j + \hat{c}(i,j), \forall(i,j) \tag{2.35}$$

This estimation process is repeated for each pixel of the image.

2.4.2 MCPU with Graph Cuts using inhomogeneous Gaussian Markov Random Field (GMRF)

Another improvement of the unwrapping problem, as it is presented at the beginning of the section, is the Multichannel Maximum a Posteriori (MAP) estimation method complemented by the use of an inhomogeneous Gaussian Markov Random Field (GMRF) as the *a priori* statistical term (2.30). This GMRF has the following expression:

$$g_\beta(h) = \frac{1}{Z(\beta)e^{-E_{prior\,\beta}(h)}} \tag{2.36}$$

On the one hand, we have the partition function $Z(\beta)$, where $\beta = [\beta_0\beta_1...\beta_n]$ is the hyperparameter vector which can represent the local spatial variation of the unwrapped heights [20]. On the other hand we have the energy function E_{prior}, which represents the relationships between pixels. This E_{prior} function can take different forms. There is the option of modeling it with a local GMRF (2.37). This solution is useful in the problematic noisy areas with big discontinuities which are the greatest point of interest in the research community. Nevertheless, the computing time is quite big because of the necessity of the hyperparameter vector estimation which requires a supplementary optimization step like the Iterated Conditional (ICM) algorithm. This ICM algorithm does not guarantee the location of the global minimums.

$$E_{prior}(h) = \sum_{p\sim q} \frac{(h_p - hq)^2}{2\beta_{p,q}^2} \tag{2.37}$$

There is another option of E_{prior} (2.38) to solve these limitations [21]. This option is based in the Total Variation model combined with a Graph-Cut-Based optimization which assure the location of the global minimum. The prior energy obtained with the TV model does not require the estimation of the hyperparamenters vector (2.38). β is a scalar and $w_{p,q}$ is 1 or $1/\sqrt{2}$ depending on the kind of neighborhood considered, and therefore the computing time is reduced considerably.

$$E_{prior}(h) = \beta \sum_{p \sim q} w_{p,q} |h_p - hq| \tag{2.38}$$

The β is a regularization parameter which give a compromise between the E_{prior} and the LF, supporting the smoothness between each pixel and its neighbors. It can be calculated with the so-called $L-curve$ looking for avoiding big changes in the *prior* with small changes in the LF and vice versa. This compromise prevents the *over-smoothing* or the *under-smoothing*. For instance, big changes in the *prior* and small in the LF can lead in the end to the MAP estimation of the *prior*. Thus, this TV model looks for not penalizing discontinuities in the function and at the same time not doing it with the smooth functions. The TV model has been used in the last decades and it is proven to be quite performant, specially when dealing with urban areas.

The last step is finally an optimization through a graph-cuts-based algorithm of the type of the one explained in the PUMA chapter (Section 2.3.1).

3 Developed algorithms and experiments

3.1 Comparison between the existing STEP unwrapping algorithms

Before undertaking the task of the joint phase unwrapping, we make a few tests with algorithms that have been already developed and performed in the STEP project. The interest of this study is simply to see the advantages and drawbacks of each of them and to have a global idea to decide which method could be better for the joint unwrapping approach.

This tests have been applied to a simulated height model, considering different baselines. We simulate a phase with the shape of a mountain of around 100m and we wrap it. The standard deviation of the considered noise is based on information of real data later used in this thesis. Note that this noise only represents thermal noise, no baseline or temporal decorrelation have been considered. To unwrap this profile we apply the three algorithms. The phase was simulated considering different baselines, and consequently, different heights of ambiguity. As it was said in the SAR Interferometry section, the size of the baseline increases the accuracy of the system, but if this size is excessively big, it appears enough decorrelation noise to deteriorate the phase disambiguation process. The bigger the baseline, the smaller the height of ambiguity. This different baselines are: 2.9 m, 14 m, 28 m and 54 m. Their corresponding intervals of height of ambiguity are: $[6, 22.5]$m,$[1.2, 4.1]$m,$[0.6, 2.1]$m,$[0.3, 1]$m.

	Growing Regions	SNAPHU	PUMA
Baseline 2.84 m	0.79867432 min	0.15849685 min	80 min
Baseline 14 m	0.81952942 min	0.15683215 min	68 min
Baseline 28 m	0.92025788 min	0.20321327 min	200 min
Baseline 54 m	0.84316146min	30 min	Too high

Figure 3.1: Comparative map[1]. Different computing times of the STEP algorithms.

The results of the the tests can be consulted in the Appendix 2. The deterioration with the large baselines is observed in all the methods and there comes a time in which the unwrapping is completely wrong. The Region Growing (RG) algorithm and PUMA give satisfactory

results until using a baseline of 28 m, when the problems start. SNAPHU is even able to unwrap correctly with this baseline of 28 m. Although it can be said that SAPHU provides better results, SNAPHU entails some noise trends, normally not producing additional unwrapping cycles.

With regard to the computational time (Fig. 3.1), it is clear that the PUMA algorithm is too slow. Since we expect the joint phase approach to increase the computing time, this algorithm is prohibitive in terms of computational burden for the multichannel unwrapping process and it is the first discard. Between the two remaining methods, the computing time in the Region Growing algorithm is more independent from the size of the baselines and the unwrapping results are not much worse than in SNAPHU. This, together with its relative ease of use, make us opting for the Region Growing algorithm as a good reference for implementing the joint approach.

3.2 Dual frequency approach

The advantages of combining different channels can be achieved with both options. However, it is preferable opting for the multi-frequency approach. On the one hand,in the *repeat-pass* air-bone acquisition mode, the multi-baseline implies uncompensated residual motion errors. They appear due to the lack of precision in the navigation system [22]. Between these errors there are azimuth registration errors and azimuth phase undulations, and they are corrected in the SAR processing (phase correction followed by a resampling) but not entirely. The problem of the multi-baseline case is that the residual errors exist and each baseline involves different residual motion errors. Nevertheless, in the case of simultaneous multi-frequency, the processed frequency bands (repeat-pass X and S) have residual motion errors, but as they are acquired simultaneously with the same baseline, these errors are virtually equal (Fig. 3.2). Thus, the combination of both bands don't increase the "intrinsic" errors and it is easier to deal with the problem. On the other hand, we need to know these baselines with a considerable precision. However, we can only achieve the precision of the inertial navigation systems, which is normally worse than the multi-frequency precision, a fraction of the wavelength [20].

Having said that, the main idea now is to take advantage of the use of different frequencies in the unwrapping process so that the combination of the data given by the different bands helps to avoid and overcome the unwrapping problems faced with the single frequency approach. The joined interferograms in this approach are the repeat-pass X-BAND and the repeat-pass S-BAND air-bone acquisitions. The X-BAND goes from 4 Ghz to 8 Ghz, which means in wave-length units from 2 to 4 cm. The S-BAND are lower frequencies, 1-2 Ghz (wavelengths from 8 to 15 cm). F-SAR permits to acquire both bands simultaneously with a vertical polarization for both bands. The unwrapping algorithm selected to develop this approach is the Region Growing algorithm, which is already coded in STEP for one frequency band. The goal is to extend it now to more frequency capabilities.

The two considered frequencies must be calibrated between them. In principle, an absolute calibration is desired. However, if there are no references available, a relative calibration in between the X and the S band is sufficient.

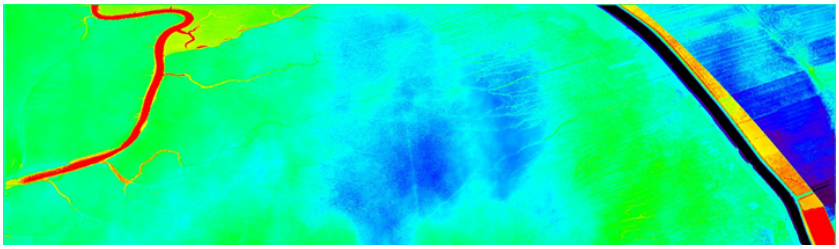

(a) Residual phase in X-BAND

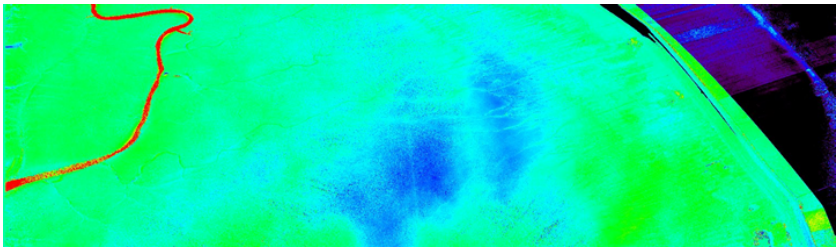

(b) Residual phase in S-BAND

Figure 3.2: Residual motion errors[2]. In the image (a) we have the residual phase in the X-BAND which is the same in the S-BAND, (b).

In (3.1) we can see the *repeat-pass* phase errors where the bs are the vertical and horizontal baseline errors. ϕ_0 is an offset.

$$\phi_{error} = (4\pi/\lambda) \cdot (b_0 + b_1 \cdot v \cdot t_{az}) \sin(\theta) - (4\pi/\lambda) \cdot (b_2 + b_3 \cdot v \cdot t_{az}) \cos(\theta) + \phi_0 \tag{3.1}$$

The errors can be estimated with the help of a reference DEM, e.g. using the single-pass calibrated phase. The calibration has to be performed prior to the phase unwrapping (using a non-linear *least-squares* estimation for example) to perform the fitting in complex domain. However, a initial estimation of the baseline error is required. An option for this initial estimation is observing the relationship between the azimuth and range frequencies (f_a, f_r) and the derivative of the expected phase error model (3.4).

$$2\pi f = \frac{\partial \phi}{\partial t} \tag{3.2}$$

$$f_{az} = \frac{1}{2\pi} \frac{\partial \phi}{\partial t_{az}} \tag{3.3}$$

$$f_{rg} = \frac{1}{2\pi} \frac{\partial \phi}{\partial \theta} \tag{3.4}$$

We divide the interferogram in blocks and consider the spectrum of each block. The location of the maximum in the blocks gives the frequencies to use in the model (3.1) and the baseline errors terms can be estimated using a *least-mean-squares* estimation. The calibration

could be done for each band. However, our main interest is the calibration of the bands in relation to each other. Normally they should be calibrated for simultaneous acquisition, but to avoid taking risks one band is assumed to be calibrated (X-BAND for instance) and the other is calibrated with respect to this reference. Of course this is not an absolute calibration and an error is being committed, but the accordance between both bands is achieved, which is the major objective.

Keeping in mind the goal of extending the existing programs based on the Region Growing algorithm to more frequency capacities, a progressive procedure has been followed. First and foremost the STEP code used for the Region Growing approach has been simply adapted to have 2 inputs /2 outputs instead of 1 input/1 output but without processing them at the same time, one band is unwrapped first and afterwards the other. No interesting modification in the algorithm has been done. As it was expected, the same results as those obtained processing individually each band with the original code are acquired.

In the next step, the option of using the coherences provided by the INSAR is added to the program. Now, the coherence used in the program can be either the one computed locally in the program out of the received wrapped phase or directly the coherence also provided by the F-SAR. As we can see in (Fig. 3.3), the results are similar. As it has been explained in the InSAR introduction this coherence is *biased*. This will be further addressed in the chapter. By now, it is sufficient to say that using big window to treat this coherence, the *bias* is partly avoided [2].

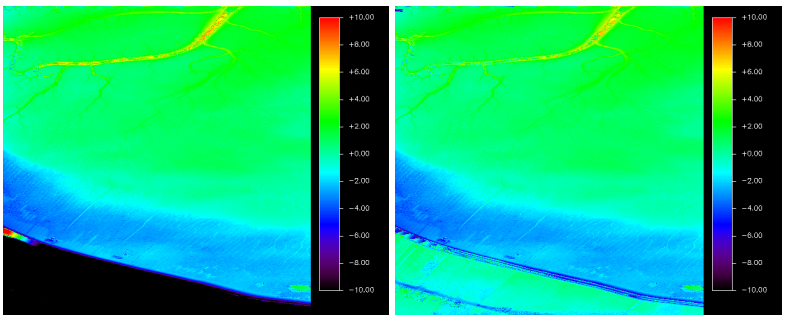

(a) Using a computed coherence (b) Using the provided coherence given by F-SAR

Figure 3.3: Unwrapping differences depending on the coherence .

3.2.1 Initial dual frequency approach

Once these first approximations are done, the first innovative attempt to achieve our goal is done. In this first incursion, the idea is to unwrap as before the phase with the higher reliability data and just to scale with the kz's into the other band. As mentioned in the previous chapters, the kz is a term that relates the absolute phase with the height and is provided by the INSAR processor (3.6). It can be seen as a phase to height conversion factor. This factor permits to scale the phases form one band to the other.

$$k_z = -(4\pi/\lambda) * Bcos(\theta - \alpha)/rsin(\theta) \tag{3.5}$$

$$\phi = k_z \cdot h \tag{3.6}$$

First of all, the coherence of both bands are compared in mean in order to select the phase of the band corresponding to the highest coherence. In our case this is usually the S-BAND. The phase in this band is unwrapped directly in accordance to the guidelines in [18], calculating the ambiguity number of unwrapping cycles (2.21) out of (2.18). Afterwards, we scale the unwrapped phase in the band of higher coherence with the kz's and we use it as a reference. This reference is used in the complex domain to reduce the fringes in the wrapped phase of the second as we see in the pseudo-code. This modified wrapped phase is unwrapped in the normal way and the reference is added again to the result to finally obtain the unwrapped phase in the second band.

$uwp1 \leftarrow RG\ normal\ unwrapping\ wp1$

$ref \leftarrow uwp1 * kz_2/kz_1$

$e^{j(wp2^{'})} \leftarrow e^{j(wp2-ref)}$

$uwp2^{'} \leftarrow RG\ normal\ unwrapping\ wp2^{'}$

$uwp2 = uwp2^{'} + ref$

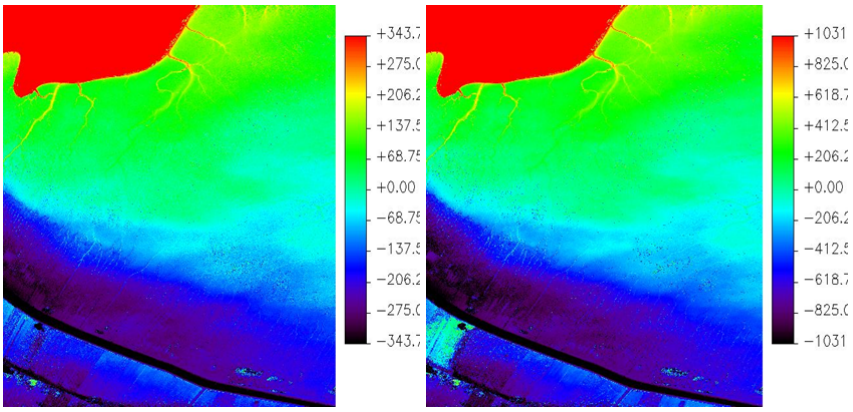

(a) Unwrapped phase S-BAND (b) Unwrapped phase X-BAND

Figure 3.4: First approach results[3]. Errors propagated from the S-BAND to the X-BAND .

The main problem of this first approach is that whenever there is an unwrapping error in the reference band, the error is propagated to the other band where maybe there is no error as it can be seen in (Fig. 3.4). That is what happens with the big error in the upper-left

corner. We can also see that the high noise in the S-BAND (light blue part) is transferred also to the X-BAND. This appears in the X-BAND as noise, but it is in fact a miscalculation of the correct number of unwrapping cycles. These *residual* errors are difficult to detect and hence, it is complicated to restore them. We refer to them as *residual propagation band-to-band* errors, avoiding the confusion with the *residual motion errors*. For these reasons, we need to improve considerably the algorithm, and for this purpose, we need to take the most of the info provided by the InSAR. It is also crucial to select the *leader* band for each pixel because the better coherence of one band in mean does not mean that that is fulfilled in the whole interferogram. The unwrapping of the bands will be from now done simultaneously.

3.2.2 Final dual frequency approach

Up till now, the benefit of using one or other frequency band has depended on the coherence. However, this coherence estimation, which is explained in the point 1.4.2 of the Introduction, can be biased [3]. The origins of this bias are mainly two:

- The interferometric phase itself is biased.
- The expectation estimator $E[]$ of the formula 2.25 is biased when dealing with low coherences.

The first problem can by rectified by the use as support of an external DEM (Digital Elevation Model) whereas the second drawback can be treated increasing the estimation window.

An additional problem is that the *bias* in the coherence is different for each frequency band, since the coherence is different. Therefore, the correct distribution of the coherence is used to try to estimate for the coherence *bias* [23]. The coherence in charge of the region creation and its growing is going to be for each pixel the highest between the X-BAND and the S-BAND coherences. Furthermore, the band that is going to lead the way in the unwrapping process is going to be determined by the standard deviation, taking in mind that it is a function of the coherence and all the *bias* considerations that this entails.

$$\sigma = \sqrt{\frac{1-\gamma^2}{2L_{int}\gamma^2}} \tag{3.7}$$

We use (3.7) when dealing with a big number of looks (L_{int}) whereas with the numerical calculation using the *pdf* when a big number of looks is not at hand.

A simple comparison in mean between the phase standard deviation in the X-BAND and in the S-BAND is worthless, because σ_S is usually lower than σ_X. This could be useful for a *multi-baseline* approach. Thus, the reasoning is as follows. Let's call ϕ_1 the phase that is unwrapped independently from the data of the other band (3.8). This relation between the band that can be unwrapped independently from the other can change in a pixel-to-pixel basis. Normally, the band that is unwrapped independently form the other is the S-BAND, but it can change.

$$\phi_1 = \psi_1 + 2\pi n_{cycle,1} \tag{3.8}$$

The wrapped phase ψ_2, on the contrary, can be unwrapped (ϕ_2) with the support of the scaled (kz_2/kz_1) unwrapping jump in ϕ_1.The estimation of the number of unwrapping cycles in the band 2 is in (3.9).

$$\hat{n}_{cycle,2} = round(\frac{\psi_2 - \frac{kz_1}{kz_2}\phi_1}{2\pi}) \tag{3.9}$$

But this does not consider the effect of noise(3.10).

$$\hat{n}_{cycle,2} = round(\frac{2\pi n_{cycle,2} + \eta_2}{2\pi}) \tag{3.10}$$

In fact, both phases are affected by noise with a certain standard deviation (3.11). This standard deviation can be called for simplicity σ_{12}, with 12 indicating that ϕ_2 has been calculated with scaled information of the band 1. Obviously, it is influenced for the single phase standard deviation of both bands.

$$\sigma_{12} = \sqrt{\sigma_2^2 + (\frac{kz_2}{kz_1}\sigma_1)^2} \tag{3.11}$$

Therefore, we can use this standard deviation to characterize a possible error in the calculation of the unwrapping cycles (η_2). We consider that $\sqrt{E[\eta_2^2]} = \sigma$. The error term should be small enough to not distort the correct result adding more unwrapping cycles. That being said, we consider a good unwrapping scene when $\sigma_{21} < 0.5 \cdot 2\pi$.

After this consideration about the standard deviations, the final approach is presented. First of all, it should be analyzed the interest of the joint frequency approach for some pixels where the unwrapping is quite complicated and the joint approach could be even more problematic than helpful. With this purpose, a noise phase estimation is calculated locally in both bands. It can be seen as a measure of the difficulty of the unwrapping process in the pixel in each band. The estimation is based in slope predictions between the considered pixel and its neighbors. If the majority of the slopes are big, the noise estimation is high. Let's call σ_1 and σ_2 the *difficulty* estimations in the participant frequency bands. When σ_1 and σ_2 are both bigger than a certain threshold, the idea is to unwrap separately the pixel in each band following the reference Region Growing algorithm. But this pixel is marked as not-properly unwrapped or invalid. The information is stored in a mask in charge of storing the successes and failures of the unwrapping process.

For the rest of the cases ,in which both estimations are lower than the threshold or one of them is lower and the other higher, the joint unwrapping itself is applied in the pixel. The less noisy band is unwrapped in the normal way with the average of the weighted slopes of the neighbors. The method for unwrapping the remaining band will be carried out depending on the next process.

Firstly, the *joint* standard deviations (σ_{12} and σ_{21}) as the one in(3.11) are calculated in the pixel in order to figure out if the first unwrapping approach (Section 3.2.1) is a good way to deal the problem. With (3.10) in mind, if the standard deviation is lower than π (in the tests a threshold of 0.8π has been used), we can take the method using the unwrapped reference

as good. The unwrapping result is going to be probably good. Of course, this happens when the error in the reference is low.

Otherwise, three different measures of the unwrapping cycles are calculated: $n_{cycle,a}$, $n_{cycle,b}$ and $n_{cycle,c}$, looking for a compromise between spatial smoothness and inter-band agreement. The second band will be unwrapped once these three measures have been considered and compared. The first measure is $n_{cycle,a}$ and is the number of unwrapping cycles if we take as unwrapping solution the one using the slope computed predictions from the phase of interest. In other words, applying single-frequency RG to the band of interest. When the neighbors are *trustful* (phase gradient between them is not big), $n_{cycle,a}$ leads to satisfactory results.

$$n_{cycle,a} = round(\frac{\psi_2 - \hat{\phi_2}}{2\pi}) \tag{3.12}$$

As in other example the ϕ_1 is the most reliable phase and the problem is in the unwrapping of the phase ψ_2. The hat in unwrapped phase ϕ_2 means that it is an estimation, not the exact one. $n_{cycle,b}$ follows the same proceeding as when the *inter-band* standard deviation is lower than π and $n_{cycle,b}$ is calculated scaling the unwrapping estimated jump phase in the good band, which is taken as reference. It does not produce big errors when σ_{ij} is not much bigger than π.

$$n_{cycle,b} = round(\frac{\psi_2 - scl_{12}\hat{\phi_1}}{2\pi}) \tag{3.13}$$

$n_{cycle,c}$ is a compromise between $n_{cycle,a}$ and $n_{cycle,b}$. The phase ψ_2 is unwrapped locally as $n_{cycle,a}$ following the normal proceedings for unwrapping postulated in [18], but using information of the already unwrapped phase for the slope calculations as a reference. This reference is finally overturned adding it in the final estimation of the number of cycles.

$$n_{cycle,c} = round(\frac{\psi_2 - \hat{\phi_{2ref}} + ref}{2\pi}) \tag{3.14}$$

Once the three measures are done, considering a neighborhood, the one giving smaller differences with the neighbors and between the X an S band is chosen as the unwrapping number of cycles for the second band following the next procedure. We calculate for the three measurment of n_{cycle} of the second band the difference between the pixel of interest and the already unwrapped neighbors (3.15). The same is done with the scaled unwrapped neighbors in the other band (3.16).

$$\bar{\phi}_{diff2,n_{cycle}} = [(\phi_{2_{i,j}} - \phi_{2_{i-1,j-1}})^2, ..., (\phi_{2_{i,j}} - \phi_{2_{i+1,j+1}})^2]^T \tag{3.15}$$

$$\bar{\phi}_{diff21,n_{cycle}} = [(\phi_{2_{i,j}} - \frac{kz_2}{kz_1}\phi_{1_{i-1,j-1}})^2, ..., (\phi_{2_{i,j}} - \frac{kz_2}{kz_1}\phi_{1_{i+1,j+1}})^2]^T \tag{3.16}$$

With this six vectors we construct (3.17), with $w \propto \frac{1}{\sigma_{12}^2}$ for diminishing the influence of bad solutions. Finally we look for the measure that minimizes $\bar{\phi}_{diff}$.

$$\bar{\phi}_{diff} = [\sum \bar{\phi}_{diff2,n_{cycle,a}} + w \sum \bar{\phi}_{diff21,n_{cycle,a}}, ..., \sum \bar{\phi}_{diff2,n_{cycle,c}} + w \sum \bar{\phi}_{diff21,n_{cycle,c}}]^T \tag{3.17}$$

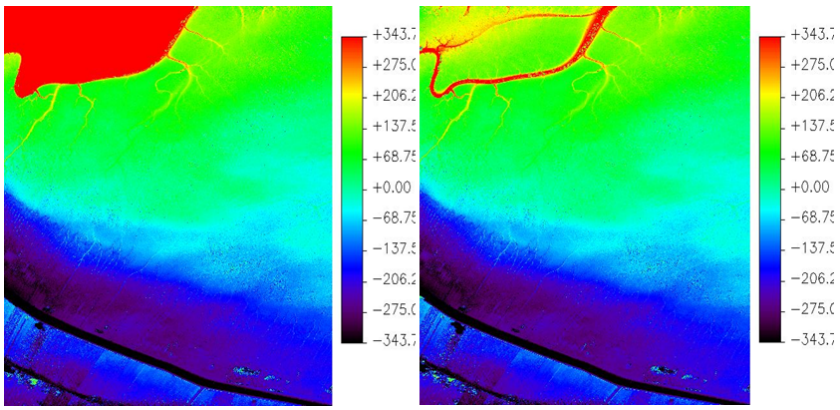

(a) Unwrapped phase S-BAND

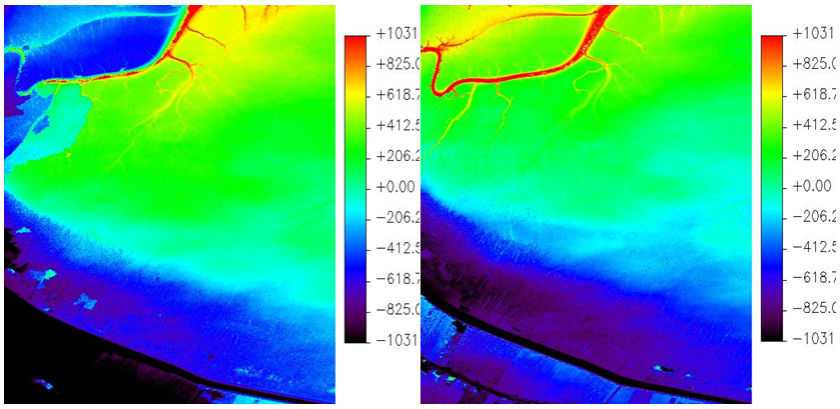

(b) Unwrapped phase X-BAND

Figure 3.5: Dual approach unwrapped phase.
[4]. In (a) there are the unwrapped phase in the S-BAND with the traditional way (left) and the unwrapped one with the definitive dual frequency approach (right). The same in (b) for the X-BAND. Even though there still some *residual* errors passing from one band to another, the improvement is important. The unwrapping error presented in (Fig. 2.2) is solved

Comparing the results of the traditional unwrapping method using one frequency and this dual approach, the improvements are notable (Fig. 3.5). The unwrapping problem on the left side of the river is solved in both bands. This is mainly due to the use of the "synthetic" coherence (the highest between the bands in each pixel). In the X-BAND, where there were more unwrapping errors, the majority of the inconsistencies have been solved. Furthermore, the noisy pattern created by the transfer of the noise from the S-BAND phase has been considerably removed. Moreover, the computing time is around the double of the time

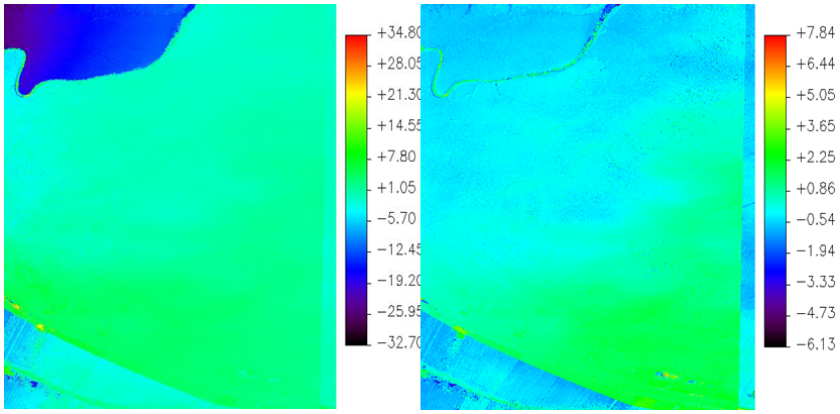

(a) Unwrapped phase S-BAND

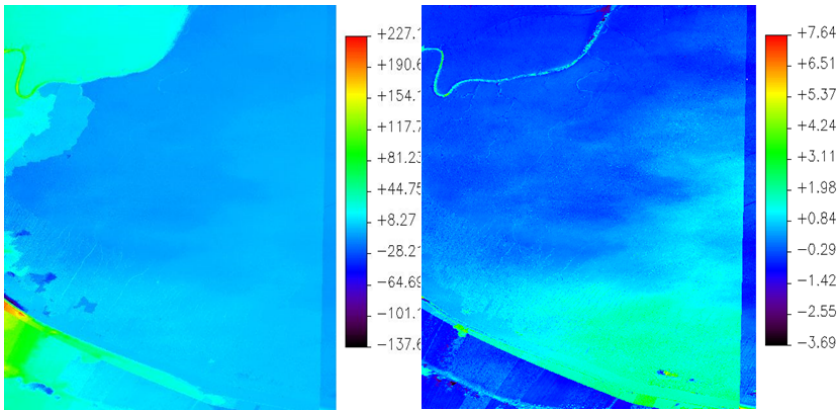

(b) Unwrapped phase X-BAND

Figure 3.6: Dual approach height comparison.

taken by the single-frequency band RG to give a solution (around 2 minutes).

Using the *phase-to-height* conversion factor kz (3.5), the Digital Elevation Models (DEMs) in the X and S bands are straightforward generated. In the problematic studied area, Jade Bight, in the north of Germany, DLR-HR counts on the help of a laser reference of the height for comparison. This allows to examine the quality of the DEM's. The DEM's obtained (Fig. 3.6) have improved with regard to the single frequency band RG algorithm. The differences between them and the laser reference is lower and it's more homogeneous around the studied area. But it cannot be denominated as perfect. We can detect an error that highlights in the meander of the river.

Coming back to the tests performed in the generated height model at the beginning of this chapter (Section 3.1). The final dual approach is applied to this simple unwrapping problem. The results are in the Appendix 2 with the rest of the tests applied to this profile. Upon a comparison between them and the new approach, the improvement in the unwrapping of this simulated height model is significant, especially as the baseline grows.

3.3 Joint MCPU statistical approach

3.3.1 First tests

For a certain frequency band, the probability density function (*pdf*) of h in a certain pixel (i, j) is given by the single-frequency likelihood function [20]

$$f(\phi|h) = \frac{1}{2\pi}\frac{1-|\gamma|^2}{1-|\gamma|^2\cos(\phi - d\frac{4\pi}{\lambda}h)}(1 + \frac{|\gamma|\cos(\phi - d\frac{4\pi}{\lambda}h)\cos(-|\gamma\cos(\phi - d\frac{4\pi}{\lambda}h)^{-1})}{(1-|\gamma|^2\cos(\phi - d\frac{4\pi}{\lambda}h)^{1/2})}) \quad (3.18)$$

Ideally, by finding the maximum of this *pdf* over a certain range (Maximum Likelihood appraoch), the height can be then reconstructed. However, this *pdf* is periodic according yo the height of ambiguity of the acquisition (analogous to a wrapped phase). By using multiple channels, this periodicity can be reduced or, ideally, eliminated. Nevertheless, in real scenarios, this situation is difficult to reach, specially when dealing with big baselines. Referring again to the simulated height model of Section 3.1, some tests have been done analyzing how complex is to identify the height of a point like for example one pixel of 113.1 m. The *multi-channel likelihood function* (composed of the LF of the repeat-pass X-BAND and the LF of the repeat-pass S-BAND) is traced firstly with a fine sampling in this pixel, considering heights separated 0.0045 m between them (Fig. 3.7). Normally discrete methods will be used for the minimums location, that is why a sampling is done. These results consider an ideal case without any noise.

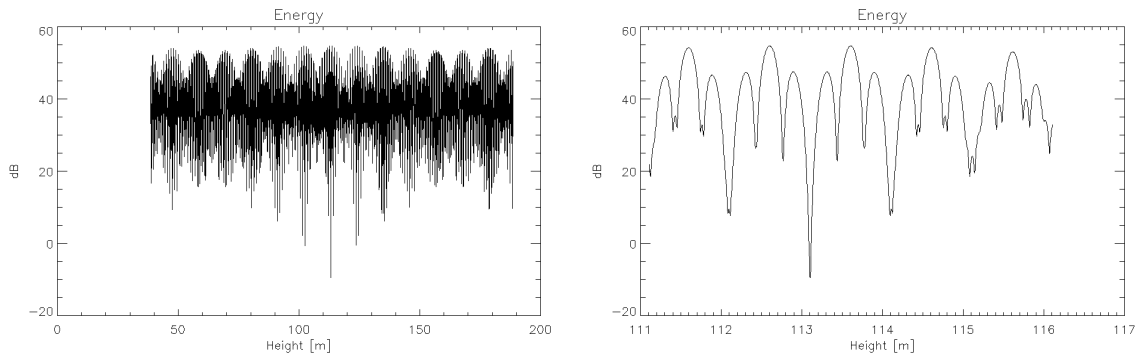

(a) Fine sample

(b) Zoomed fine sample

Figure 3.7: Fine sample.

The peak around 113.1 is well identified but if the image is zoomed, we can see that the peak is narrow (around 20cm). Therefore, using a coarser sampling more realistic in terms of computational time (0.45 m) the energy profile is completely distorted and ambiguous. Moreover, even if a fine sample is considered, when we introduce some noise, the single channel energies are shifted and the resulting energy is completely distorted.

This is exactly what it is shown in (Fig. 3.8) when no global minima can be identified. It is a big deal to locate the global minimum between these solutions and there are big possibilities

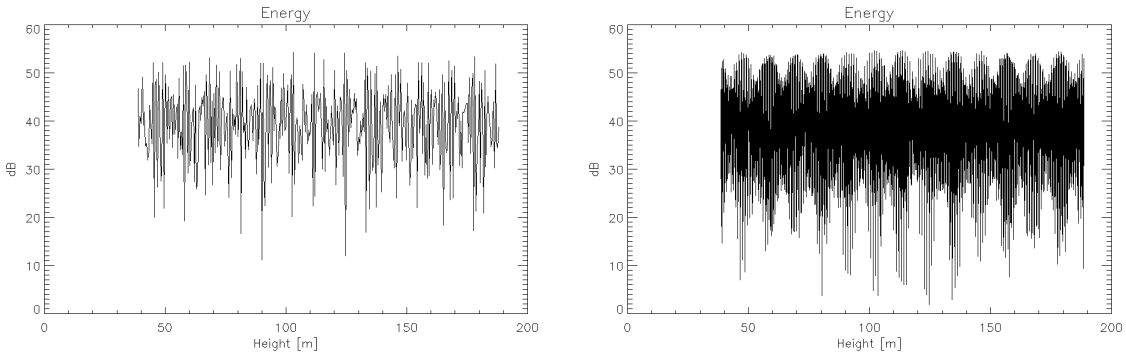

(a) Coarse fine sample

(b) Fine sample plus noise

Figure 3.8: More realistic samples

of choosing one peak that is only a local minimum. Either with a discrete (*graph-methods*) or a continuous (*simulated annealing*) optimization, the good solution is not guaranteed.

In theory, the combination of different bands in the statistical method can help to facilitate the statistical process. In fact, as it has been presented in the Section 4.2, the combination of multiple likelihood functions can eliminate the periodicity of the *single-frequency pdf*, canceling annoying peaks. However, in practice things are not so simple and to have an understandable and unambiguous energy profile normally we need some extra spatial information. This will be seen in the MCPU (Multi Channel Phase Unwrapping) methods developed in the next points.

3.3.2 Joint MCPU (Multi Channel Phase Unwrapping)

The second option for the combination of both *repeat-pass* interferograms in the X and in the S band is the Multichannel Phase Unwrapping approach (Section 2.4). In this case the *multi-channel* is achieved with the two frequency bands. Its major advantage over the previous approach is that it calculates the h directly, not the unwrapped phase, which could be interesting for the DEM constructions. This solution is more daring than the Region Growing dual approach. In the HR-DLR institute, the data is provided by the air-crafts with a height of ambiguity small enough to turn this method more complicated. The *residual motion errors*, have a bigger impact than in the Region Growing case, since they will shift the *pdf* of each considered channel.

The implementation started using as reference one program already coded in the HR-DLR institute. The program computes the algorithm presented in [20] and explained in the Section 2.4.2, using as the E_{prior} (of the inhomogeneous Gaussian Markov Random Field (GMRF) modeling an *a priori* knowledge of h) the TV-model (2.38) and an optimization via *graph-cuts*. The first change has been including in the code the Local Plane Parameters Estimation (LPPE) [19] method already presented in the Section 2.4.1. In this way and considering the X-BAND and the S-BAND as the channels involved in the *multi-channel* term, the formula(3.19) gets

$$F_{mf}(\Phi|h) = \prod_{n=1}^{2} f(\phi_n) \tag{3.19}$$

with ϕ_1 and ϕ_2 the phase acquired in the X and in the S-band. The exact formula of f_{ϕ_n} (2.32 and 2.33) is repeated here to simplify the reading

$$f(\phi_n(p,q)|x_{ij}) = \frac{1}{2\pi}\frac{1-|\gamma_n|^2}{1-|\gamma_n|^2\cos(\phi_n(p,q)-d\frac{4\pi}{\lambda_n}(ap+bq+c))}x(1+K) \tag{3.20}$$

$$K = \frac{|\gamma_n|\cos(\phi_n(p,q)-d\frac{4\pi}{\lambda_n}(ap+bq+c))\cos(-|\gamma_n\cos(\phi_n(p,q)-d\frac{4\pi}{\lambda_n}(ap+bq+c))^{-1})}{(1-|\gamma_n|^2\cos(\phi_n(p,q)-d\frac{4\pi}{\lambda_n}(ap+bq+c))^{1/2})} \tag{3.21}$$

The computing time of the reference code is quite big, specially in comparison with the time required by the Region Growing algorithm. However, in the case of including the LPPE for the height reconstruction of one pixel, it analyzes not only the likelihood function for the considered pixel (i,j) but also the function for N_c-1 positions more. N_c-1 is the number of the adjacent pixels considered for the h_{ij} estimation (N_c could be 5 or 9 for example). As a result of this fact, it is assumed that the computing time will increase. Not only that, but now the height estimation is not just an estimation of the h itself. Now, conversely, it is necessary the estimation of three plane parameters a, b and c (3.22) to compute the height h by $h_{ij} = a(\hat{i,j})i + b(\hat{i,j})j + c(\hat{i,j})$.

$$\hat{x_{i,j}} = [a(i,j)b(i,j)c(i,j)]^T = argmax \prod_{(p,q)\in N_{ij}} F_{mf}(\phi(p,q)|x_{i,j})g_\beta(h) = \prod_{(p,q)\in N_{ij}}\prod_{n=1}^{N} f(\phi(p,q)|x_{i,j})g_\beta(h) \tag{3.22}$$

where $g_\beta(h)$ is the GMRF(2.38 and 2.36).

The estimation of the three plane parameters entails the need to perform an optimization algorithm able to locate the global minimum between a large number of local minimums. Here it comes our second innovation applying a *simulated annealing* optimization (Appendix 1). The *pseudo-code* of this algorithm has been coded in IDL. The developed *simulated annealing* algorithm has been tested is some profiles with many local minimums. With a sufficient number of iterations, it finds the global minimum and it does not get stuck in a partial solution. Even so, the computational time required by these simple tests is big considering that this time grows exponentially if it is applied to the problem in which we are interested in. It has not been possible to adapt the *simulated annealing* algorithm to the MCPU with feasible time results. But the problem is rather the non-convexity of the function 3.22, together with the noise presence, that turns the unwrapping problem into an almost impossible task. Therefore, the discrete solution using *graph-cuts* is preferable.

3.3.3 STEP statistical algorithm improvement

The STEP existing algorithm, calculates the h directly with a MAP (Maximum A Posteriori) estimation (2.30) where the prior probability of h is $g_\beta(h)$ (2.36) and the energy funcion E_{prior} expressing the relationship between the pixels is computed with the TV model (2.38). This *prior* is what gives the smoothness between the pixels and its neighbors with a regularization parameter β. All the previous is combined with $graph - cuts$ optimization algorithms.

The main issue of this algorithm is that, even with the prior, the combination of the X-BAND and the S-BAND is not enough to solve the ambiguities of the Multi-channel Likelihood Function (MLF). To deal with a problem possible to tackle, it would be interesting to limit the search interval for the height. This selection of the search interval will be based on a previous h estimation out of the calibrated unwrapped phase obtained with a *single-pass* acquisition in the X-BAND. We must recall that this F-SAR provides simultaneously *repeat-pass* and *single-pass* acquisitions.

The beginning of the process is to remove as much noise as possible from the *repeat-pass* acquisitions. In order to do this, the complex phase in the X and the S bands are filtered with an Anisotropic Filter [24]. The filter is applied to the complex phases so the noise is reduced on homogeneous regions, the weak edges are preserved and the hard targets are kept intact. The main idea to use this filter is then to remove the noise and to reduce the edges. This statistical approach is less sensitive to the edges than the RG approach where a tiny change in them could lead to an erroneous number of unwrapping cycles. On the other hand, the filter is going to reduce the resolution of the image. Before applying the filtering, the resolution is of 0.5 m both in azimuth and in range and then is of 2 m. Nevertheless, it is not harmful for our approach where so much precision is not necessary.

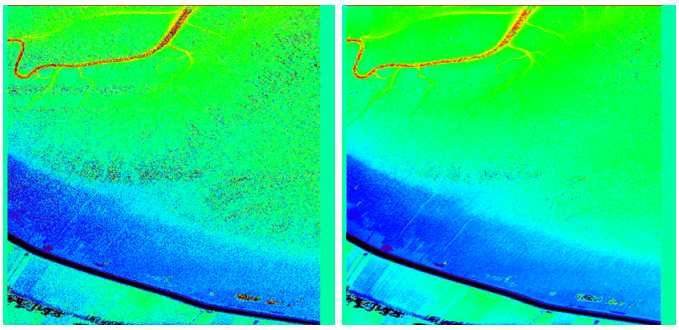

(a) X Single-pass phase previous filtering

(b) X Single-pass phase post filtering

Figure 3.9: Example of the effect of the Anisotropic Filter .

The calibrated unwrapped phase (and hence the height estimation) from the X *single-pass* acquisition passes also through this filter with the intent to reduce also the noise to make the selection of the height search interval of each pixel more clear. In (Fig. 3.9) the effect in the *single-pass* phase is shown. The phase noise after the filter is clearly smoother.

At this point, on the *repeat-pass* side, the phases are calibrated in the same way than in the RG approach. On the *single-pass* side, the limitation of the search interval is finally carried

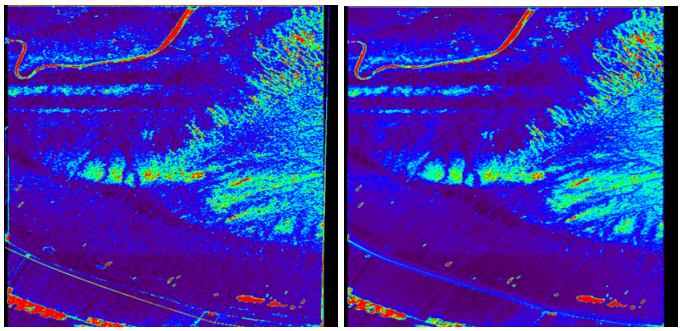

(a) Height standard deviation reference model (b) Hiehgt standar deviation of the filtered X single-pass DEM

Figure 3.10: Height standard deviation comparison.

out. The selected interval depends on the height standard deviation σ_h of the filtered *single-pass* DEM. In the area of study (the same tested in the RG approach), there is a laser height reference of the terrain. Therefore, the σ_h can be compared with the real standard deviation of the height (Fig. 3.10). In the image we can observe that the agreement between both standard deviations is quite good and hence the height interval selection can be considered as reliable.

In the interval selection we take also into account an offset (in this experiment equal to 1 m) (3.23). This offset intends to accommodate the uncompensated *residual motion errors*, which are not present in *single-pass* phase, but might be found in the *repeat-pass* one.

$$h - (2\sigma + off) < \hat{h} < h + (2\sigma + off) \tag{3.23}$$

In the image (Fig. 3.11), the example of the height interval selection shows how the complexity of the peak location has been reduced substantially.

Just after the limitation of the search interval, the next step is to find a regularization parameter β, using the interval and the *repeat-pass* phases. The objective is to achieve a compromise between the prior and the likelihood function, avoiding either an over-smoothing or a under-smoothing. Relying on the so-called *L curve* we get a regularization parameter β of 0.01 (Fig. 3.12) [25].

Once we have the *repeat-pass* phases, the height search interval and the regularization parameter β, it is only needed to carry out the optimization step itself. For each pixel, the likelihood function and the prior are calculated. And they are given as inputs to the optimization algorithm via *graph-cuts* to finally achieve a good height estimation. The optimization algorithm needs to consider for each pixel not only its position (azimuth and range dimensions) but also the search interval of height for both bands. The data storage for each individual pixel is huge and thus, the process of the interferogram is divided in blocks for efficiency reasons. It is consider an overlap of 10% between the blocks in order to avoid possible offsets.

After all the steps of the previous process have been completed, the dual-frequency band DEM is obtained. We can state with certainty that the unwrapping process is quite successful.

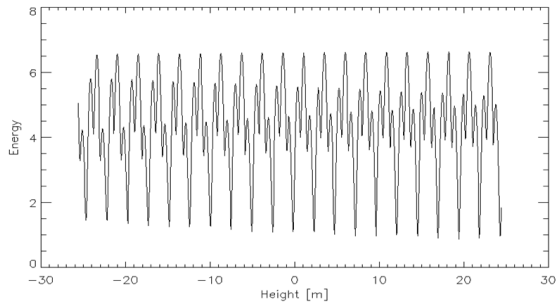

(a) Search interval before limiting it

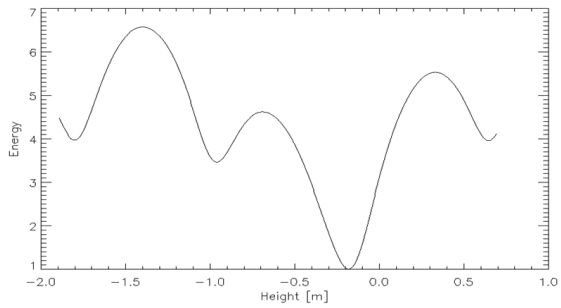

(b) Search interval after limiting it

Figure 3.11: Search interval of height limitation[5].

It is true that there are some pixels that are not correctly reconstructed but this is due to a limitation of the algorithm. There are still some pixels which, after the whole process, have a height interval of search with more than one optimum and consequently, its correct height is not founded. In (Fig. 3.13) we have the obtained DEM and a comparison between this DEM and the height laser reference of the area. The difference is negligible except for some residual motion errors and the above named erroneous pixels.

We can also compare the obtained DEM with the one estimated with the *single-pass* acquisition (Fig. 3.14). The model has been improved in terms of noise as it was expected.

A last note can be done with respect to the computing time. This statistical approach is much more *heavy* than the RG one. Around 50m are needed to complete the height reconstruction of the tested area.

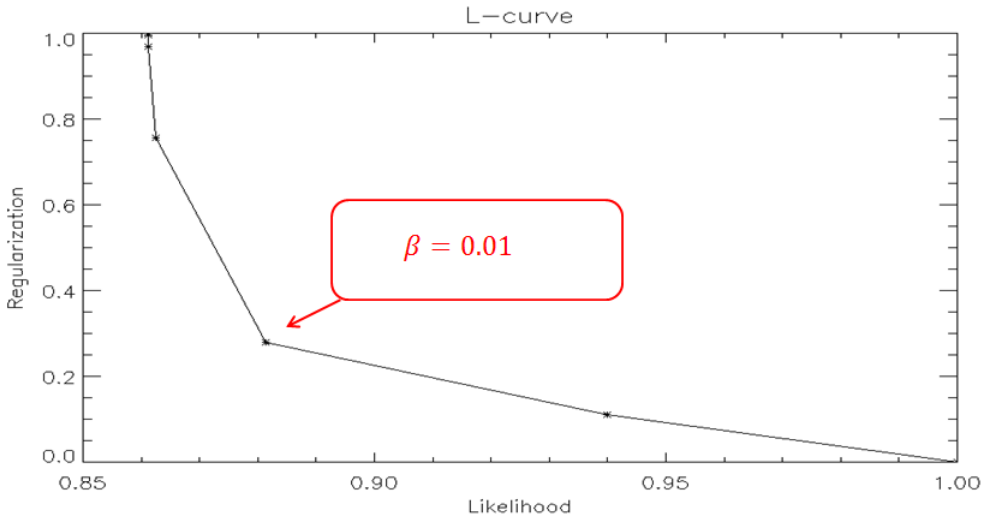

Figure 3.12: Prior regularization[6].

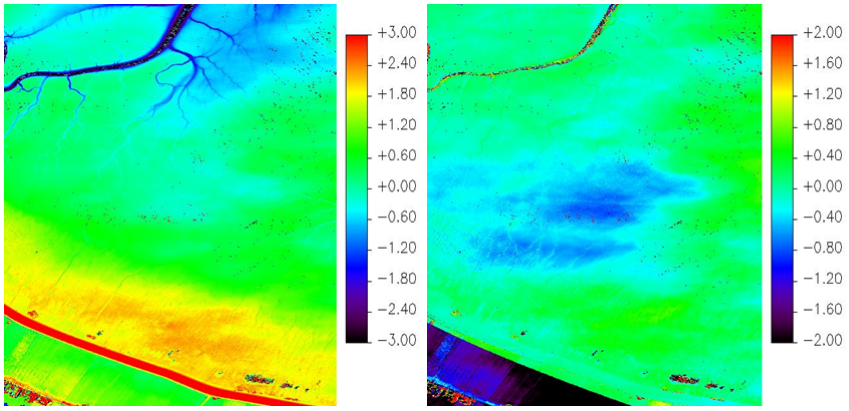

(a) Digital Elevation Model

(b) Difference between the obtained DEM and the laser reference

Figure 3.13: Dual frequency band statistical approach results .

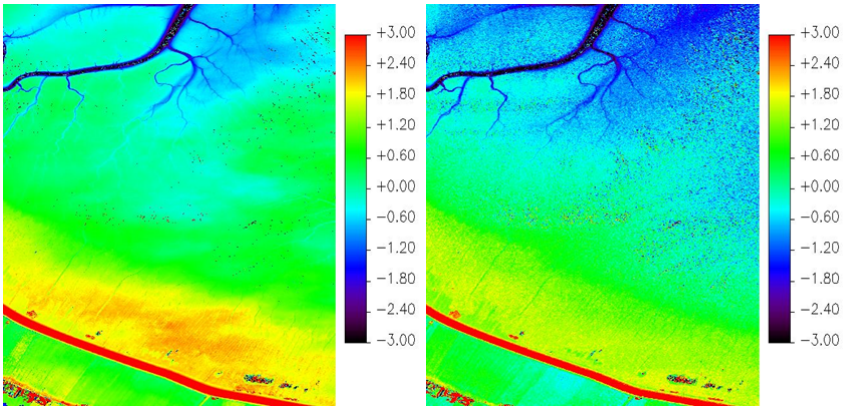

(a) Joint phase repeat-pass DEM (b) X-band single-pass DEM

Figure 3.14: Comparison between single-pass and repeat-pass DEM .

4 Conclusion

First of all, the idea that leads to the development of multi-channel phase unwrapping methods is the limitation on the single-pass ones with big baselines and hence with small heights of ambiguity. This limitation has been demonstrated with the first tests in the thesis. Here there are the conclusions we draw from the to implemented approaches and a comparison between them.

There are different conclusions that can be drawn from the first joint approach based on the extension of the growing regions algorithm. First and foremost, we face the dilemma of developing the multichannel approach with different baselines or with different frequency bands. As it has been commented several times in this thesis, the $repeat - pass$ InSAR mode which is the one mostly used here in the institute, has an important characteristic which is the presence of residual motion errors. The origin of these errors lies in the inaccuracies of the navigation system. These errors change between the different baselines exacerbating the problems. For the multi-frequency case based on the combination of the X-BAND and the S-BAND, the residual motion phase is the same because they are acquired at the same time. Therefore the unwrapping problem is more easily treated and we come to the conclusion that it is better to address the problem with the frequency approach.

Even if all of these considerations are important, the key of achieving a performant and interesting joint phase unwrapping process is to discover in every pixel which frequency band is able to give an accurate solution. What is more, the algorithm must know how two combine the information of the two bands when this is convenient and to develop some alternative treatment plan when the information of both bans is not reliable. This has been the main goal of all the methods developed in this thesis in which phase/height standard deviations and slope predictions have been applied to analyze all the previous alternatives. It is important to keep in mind that all these measures are *biased* as they are estimations. With a sufficient number of looks this bias can be faced.

The developed dual Region Growing algorithm has greatly improved the unwrapping results, proving to be an important tool for the generation of highly accurate elevation models [26]. It was not only able to reduce the number of wrongfully unwrapped regions, but also to reduce considerably the noise transferred from one band to the other. Naturally, since the process is based on possibly biased estimations, there might be still be some small transfer of noise, but far less significant, as shown by the real data results. One last important thing to note is that the computing time is around the double (around 2 min) of the time required by the single-frequency band Region Growing algorithm, which is already a very efficient algorithm in time. Consequently, this new joint phase method is not going to be problematic in terms of the computing time.

On the other hand, the multichannel statistical approach has been improved. As we said,

there are some MAP (Maximum a Posteriori) methods working with the likelihood function of the phase and optimized with some *prior* spatial information. However, there are not enough to give an energy profile without ambiguities in the case of combining the *repeat-pass* X-BAND and S-BAND, and even with *graph cuts* algorithms the optimum of this profiles (giving us directly the good height of the pixel) are not found. This is the reason why we have taken advantage of the *single-pass* acquisition in the X-BAND which can be acquired simultaneously with the *repeat-pass* acquisitions. The calibrated unwrapped phase (or the height estimation with the kz) of the *single-pass* can help us to reduce the ambiguity limiting in each pixel the height search interval. Moreover , a regularization has been carried out to obtain a compromise between the *prior* and the likelihood functions. With these changes, a high resolution DEM is constructed. There are still some pixels in which the height search interval has more than one peak. Nevertheless, the solution if is compared with the one obtained with the traditional methods is good and these errors in some pixels could be solved upgrading the *prior* and the limitation of the search of interval. The extension of the algorithm to more channels is also expected to give even better results. This statistical approach is much more "heavy" with respect to the computational time. It takes around 50 minutes to finish.

Finally, if we should have to choose between the two joint phase implemented approaches, it would be better to opt for the extension of the RG algorithm. The results are better with this approach and particularly the computing time is more than twenty times smaller. However, if the intention is to extend the algorithm to more channels, the approach that should be taken as reference would be the statistical one. In that case, the effect of having a Multi-Likelihood function made of more independent channels could really contribute to find a global solution. Furthermore, this extension would be easier than for the RG case where the use of more acquisitions is limited.

Appendix

Appendix 1: Simulated Annealing Algortihm

Finding an optimal solution for certain non linear optimization problems can become a very difficult task. This happens when the problem solution can be located in a large range. Even with the modern computing power capacities there are still too many solutions to consider and the optimization algorithms can get stuck in a local solution and not in the global one. One of the most performing ways to find the global solution is the simulated annealing algorithm.

The simulated annealing algorithm is originally inspired from the process of metal annealing. The idea was first published by Metropolies in 1953. The annealing consists in heating and cooling a metal with the intention of altering the energy and structure of the material. The metal is first heated to reach the melting point and then it is cooled. If the cooling process is carried out too quickly, the result will be a metal containing imperfections. If the cooling process is slow enough, this imperfections won't appear. When this is achieved, we get the minimum energy state.

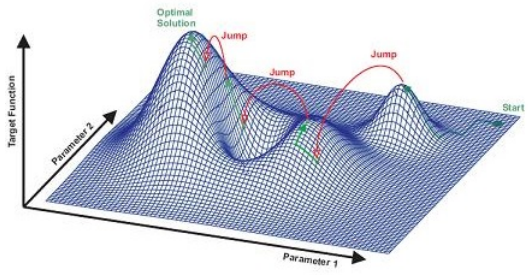

Figure .1: Simulated Annealing[1]. With the simulated annealing method, the optimization process does not get stuck in local optimums, discarding local optimums as the temperature cools. In this image the jumps from local optimums is represented.

The simulated annealing copies this procedure and keeps a temperature variable and simulates this cooling process. A high temperature variable is set at the beginning of the process and it is reduced progressively. When this temperature is high the probability and frequency of accepting wrong solutions is big. This permits to the algorithm to jump and finally rejects local optimums that finds in the first steps of the execution. As the temperature is reduced, the probability of accepting local solutions is reduced as well, and that is what allows the algorithm to focus on the correct area and to find the optimal solution. When the optimal solution is located, the process is in the frozen state. Therefore, this process is very useful when dealing with large problems with a big number of local optimums. The pseudocode of the algorithm is as follows

$Input : ProblemSize, iterations_{max}, temp_{max}$

$Output : Sbest$

$Scurrent \leftarrow CreateInitialSolution(ProblemSize)$

$Sbest \leftarrow Scurrent$

$for\ (i = 0\ to\ iterations_{max})$

$Si \leftarrow CreateNeighborSolution(Scurrent)$

$temp_{curr} \leftarrow CalculateTemperature(i, temp_{max})$

$if\ (cost(Si) \leq cost(Scurrent))$

$Scurrent \leftarrow Si$

$if\ (cost(Si) \leq cost(Sbest))$

$Sbest \leftarrow Si$

$endif$

$elseif\ (exp(\frac{Cost(Scurrent)-Cost(Si)}{temp_{curr}}) > Rand())$

$Scurrent \leftarrow Si$

$endif$

$endfor$

$Return(Sbest)$

Appendix 2: Simulation in a created height model: results

Here in the Appendix 2 we find the results of the tests that have been carried out in the wrapped phase in the X-BAND of a simulated synthetic height model (Fig..2). This height model has a maximum height of around 100 m and it has some noise coming from real data measures in the X-BAND (standard deviation around 0.7). To unwrap the wrapped phase of this model (Fig..4), the three unwrapping algorithms existing in STEP (RG, SNAPHU, PUMA) have been applied to this phase with different baselines, and consequently, different heights of ambiguity (Fig..3).

We find the unwrapped phases for the three algorithms and in each of them for the four baselines. The results are in (Fig..5) for the Region Growing algorithm, in (Fig..8) for SNAPHU and in (Fig..11) for PUMA. On the other hand, scaling this unwrapped phase with the kz, the obtained heights can be compared with the initial height. The results of this comparison for the RG, SNAPHU and PUMA cases are shown respectively in (Fig..6), (Fig..9) and (Fig..12). The same if we want to see the differences between the initial phases and the obtained ones: (Fig..7) for RG, (Fig..10) for SNAPHU and (Fig..13) for PUMA.

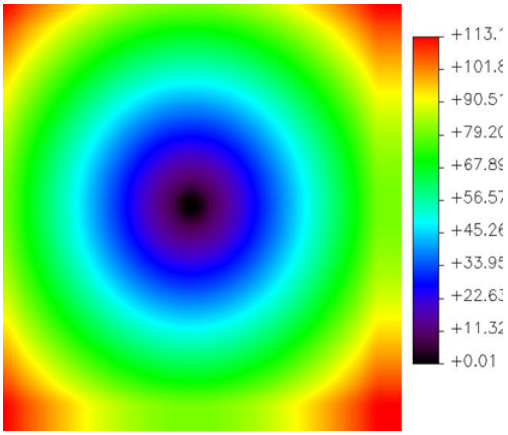

Figure .2: Ideal profile[2].

Baseline	2.9 m	14 m	28 m	57 m
HoA	[6, 22.5]m	[1.2, 4.1]m	[0.6, 2.1]m	[0.3 , 1]m

Figure .3: Tested Baselines and HoAs[3].

On the other hand, the same experiment has been done with the developed dual frequency approach of the RG algorithm. The results of the unwrapped phases, the height differences and the phase differences are in (Fig..14), (Fig..15) and (Fig..16).

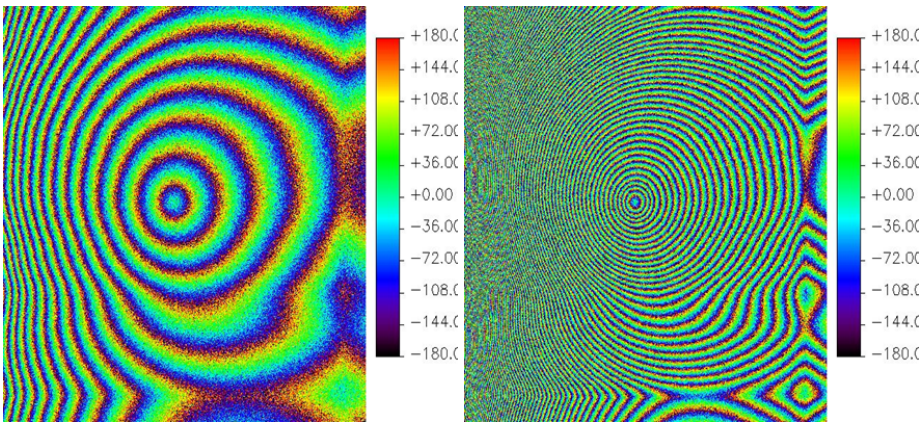

(a) Wrapped phase baseline 2.9 m

(b) Wrapped phase baseline 14 m

(c) Wrapped phase baseline 28 m

(d) Wrapped phase baseline 57 m

Figure .4: Wrapped phases.

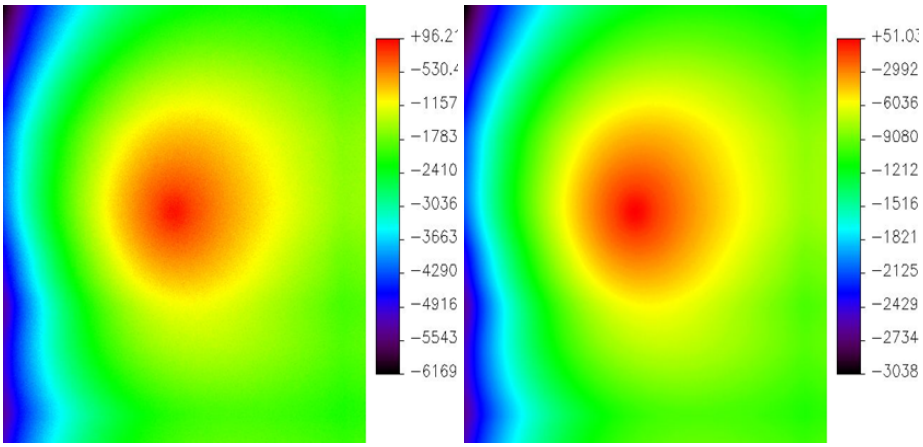

(a) Unwrapped phase baseline 2.9 m (b) Unwrapped phase baseline 14 m

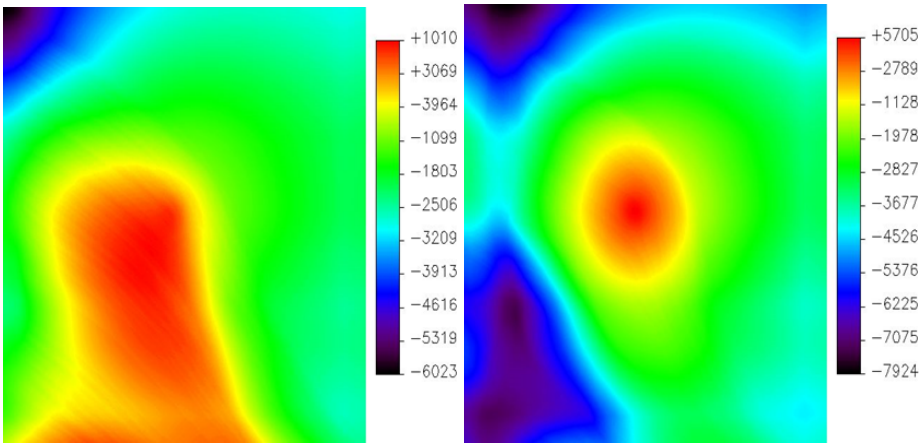

(c) Unwrapped phase baseline 28 m (d) Unwrapped phase baseline 57 m

Figure .5: Phase Unwrapping solutions with the Region Growing algorithm.

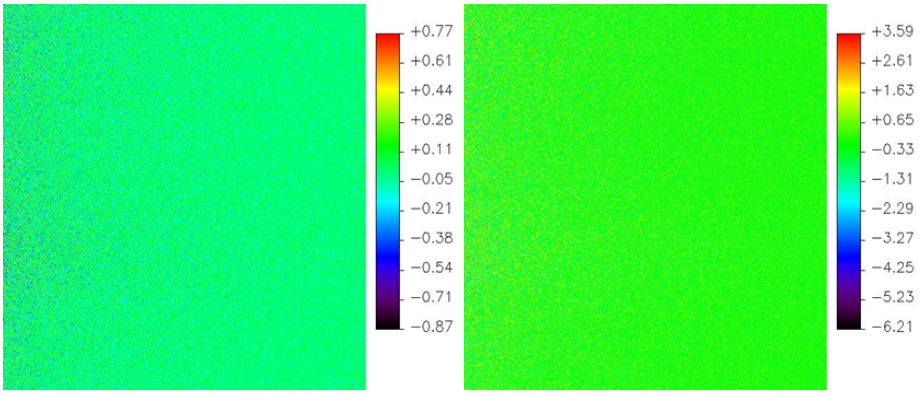

(a) Height difference baseline 2.9 m (b) Height difference baseline 14 m

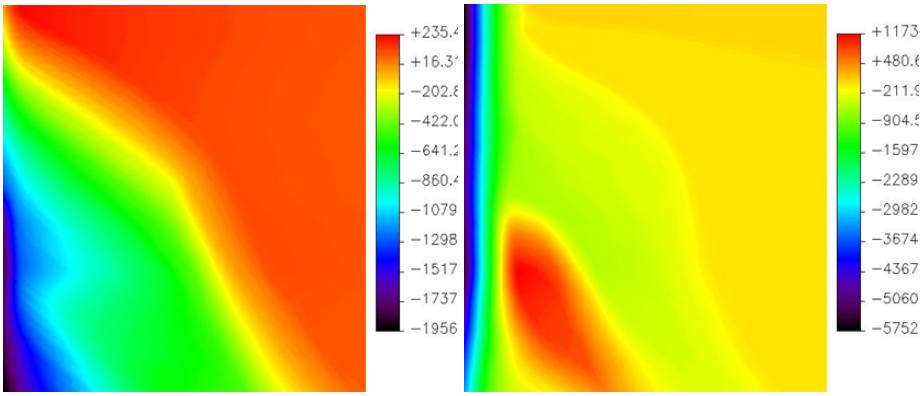

(c) Height difference baseline 28 m (d) Height difference baseline 57 m

Figure .6: Differences between the height obtained with the Region Growing algorithm and the initial one.

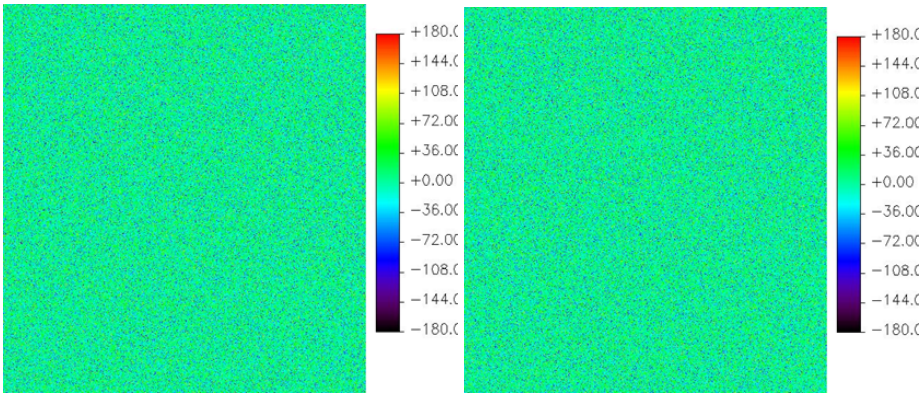

(a) Phase difference baseline 2.9 m (b) Phase difference baseline 14 m

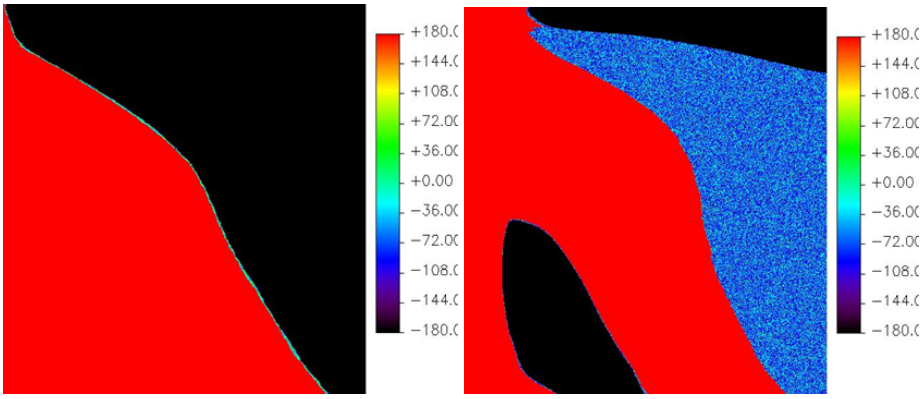

(c) Phase difference baseline 28 m (d) Phase difference baseline 57 m

Figure .7: Differences between the phase obtained with the Region Growing algorithm and the initial one.

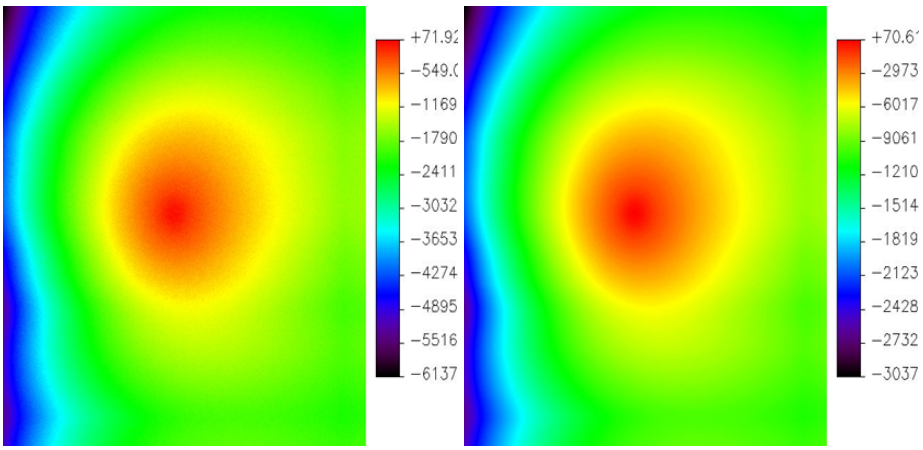

(a) Unwrapped phase baseline 2.9 m (b) Unwrapped phase baseline 14 m

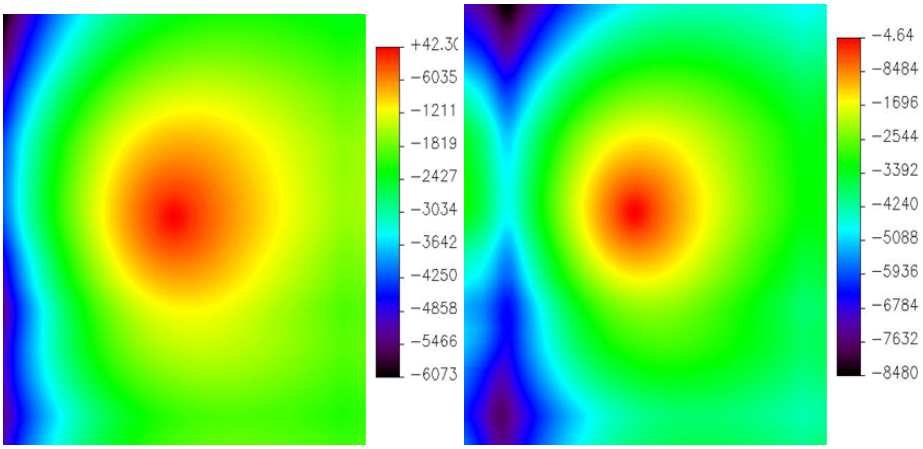

(c) Unwrapped phase baseline 28 m (d) Unwrapped phase baseline 57 m

Figure .8: Phase Unwrapping solutions with SNAPHU.

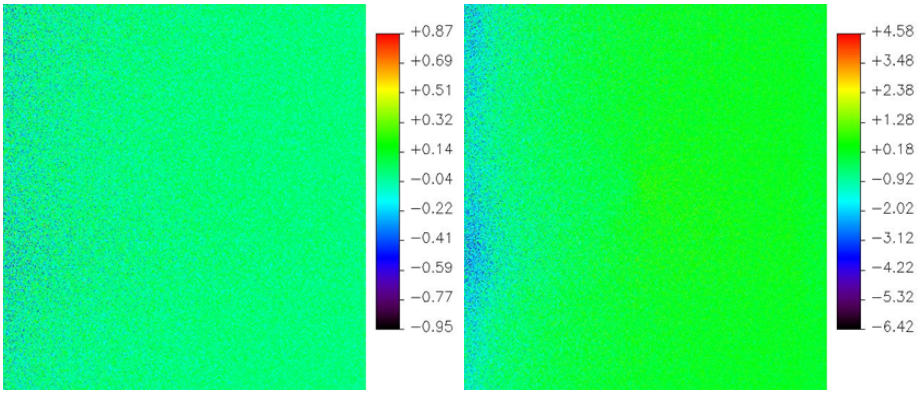

(a) Height difference baseline 2.9 m (b) Height difference baseline 14 m

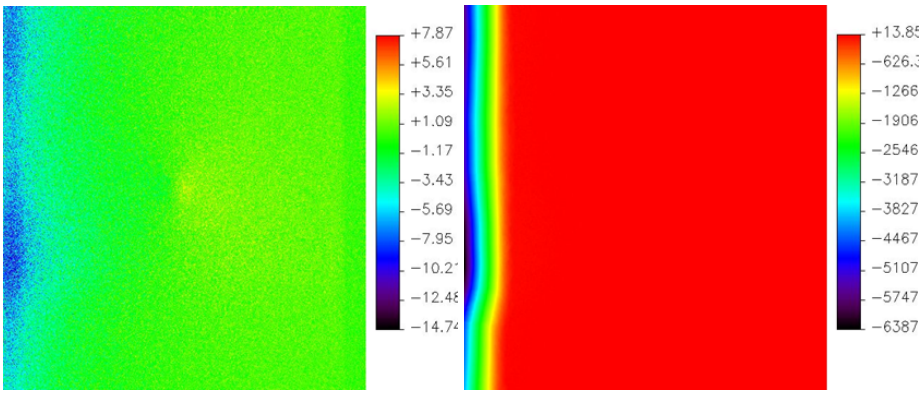

(c) Height difference baseline 28 m (d) Height difference baseline 57 m

Figure .9: Differences between the height obtained with SNAPHU and the initial one.

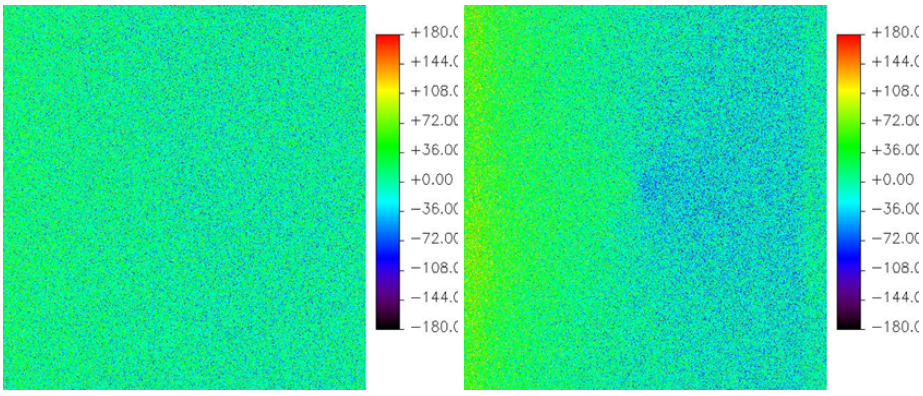

(a) Phase difference baseline 2.9 m (b) Phase difference baseline 14 m

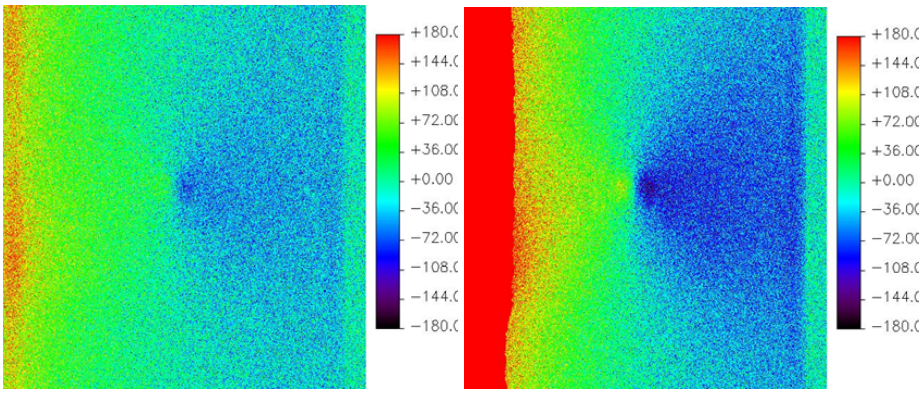

(c) Phase difference baseline 28 m (d) Phase difference baseline 57 m

Figure .10: Differences between the phase obtained with SNAPHU and the initial one.

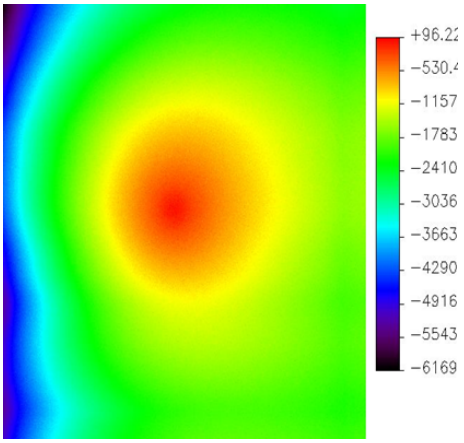

(a) Unwrapped phase baseline 2.9 m

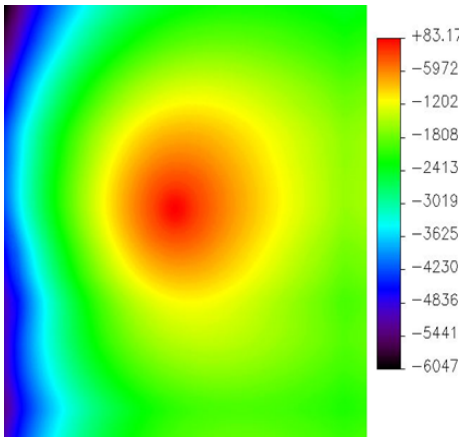

(b) Unwrapped phase baseline 14 m

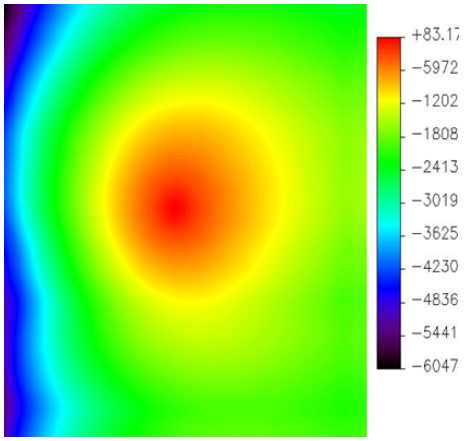

(c) Unwrapped phase baseline 28 m

Figure .11: Phase Unwrapping solutions with PUMA.

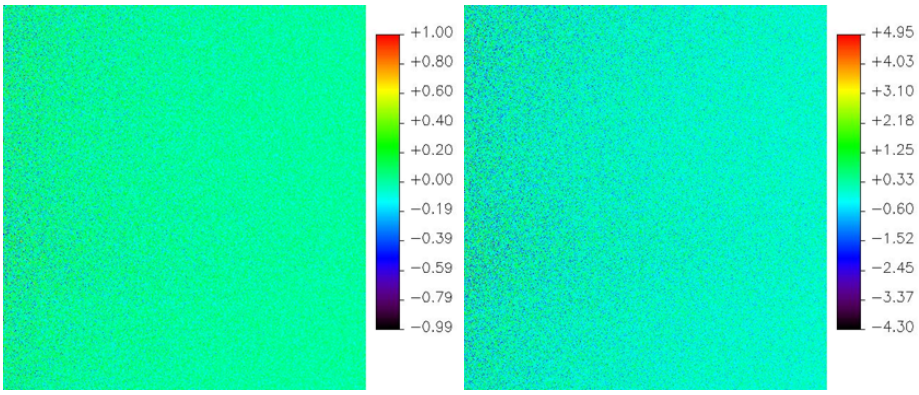

(a) Height difference baseline 2.9 m (b) Height difference baseline 14 m

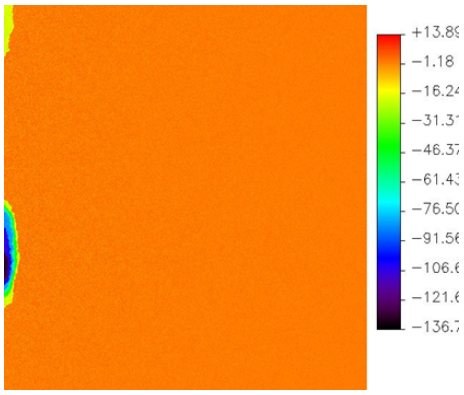

(c) Height difference baseline 28 m

Figure .12: Differences between the height obtained with PUMA and the initial one.

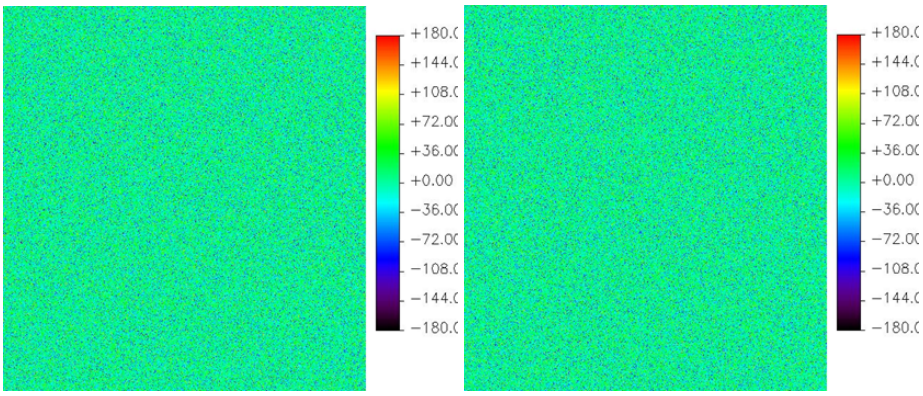

(a) Phase difference baseline 2.9 m (b) Phase difference baseline 14 m

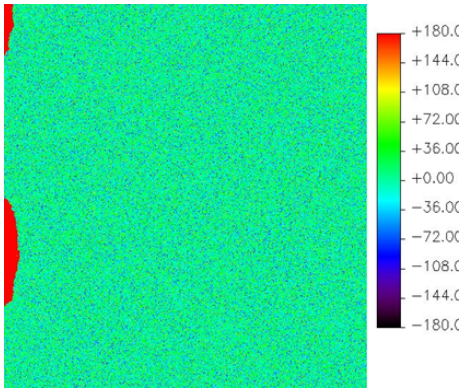

(c) Phase difference baseline 28 m

Figure .13: Differences between the phase obtained with PUMA and the initial one.

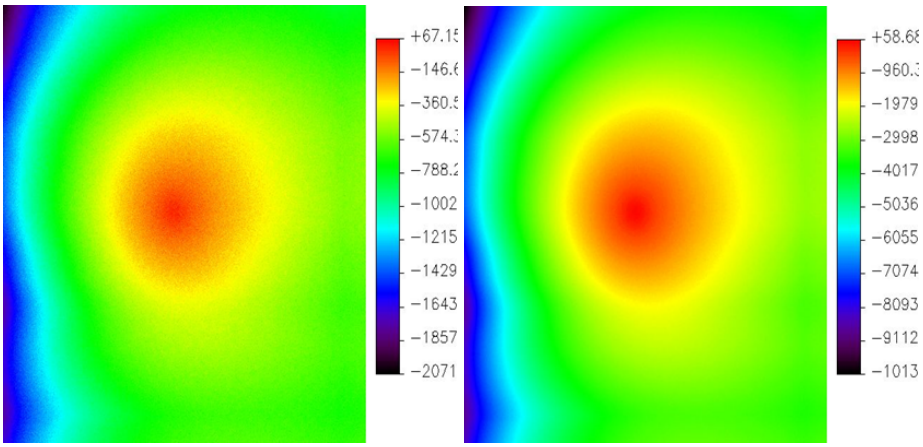

(a) Unwrapped phase baseline 2.9 m (b) Unwrapped phase baseline 14 m

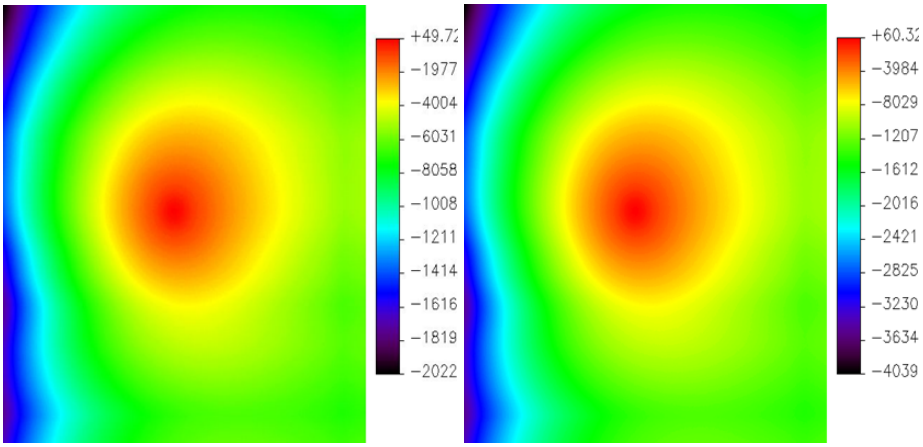

(c) Unwrapped phase baseline 28 m (d) Unwrapped phase baseline 57 m

Figure .14: Phase Unwrapping solutions with the dual frequency approach of the RG algorithm.

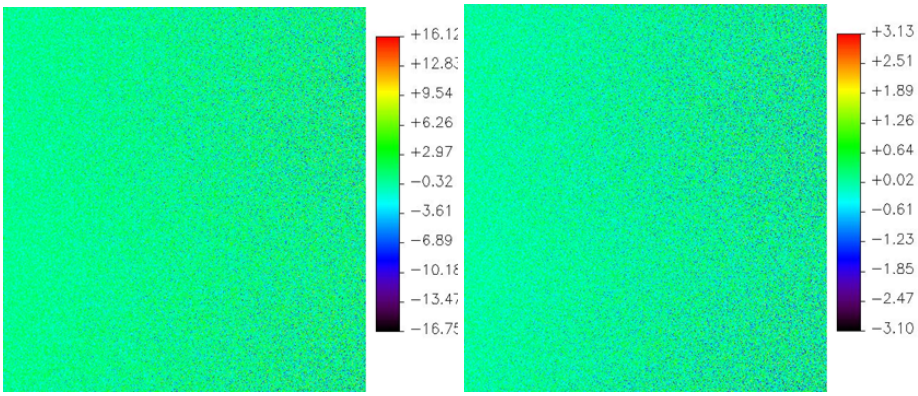

(a) Height difference baseline 2.9 m (b) Height difference baseline 14 m

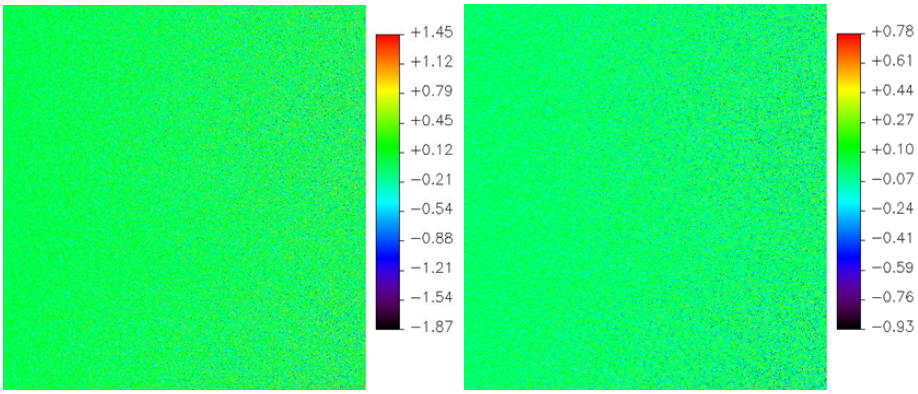

(c) Height difference baseline 28 m (d) Height difference baseline 57 m

Figure .15: Differences between the height obtained with the dual frequency approach of the RG algorithm and the initial one.

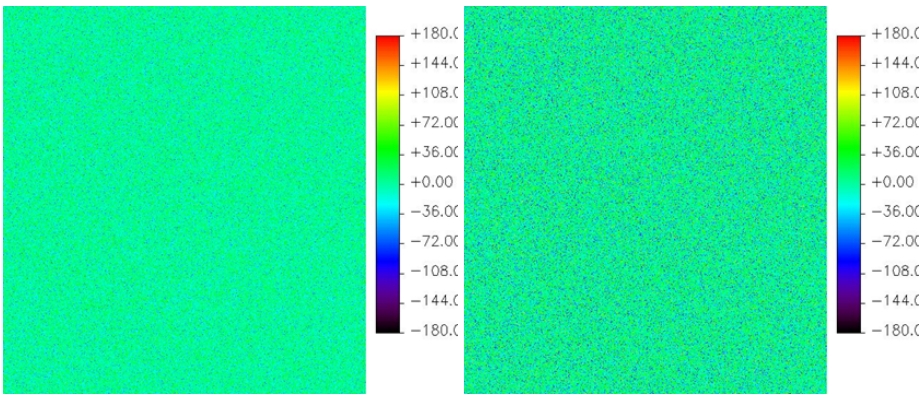

(a) Phase difference baseline 2.9 m (b) Phase difference baseline 14 m

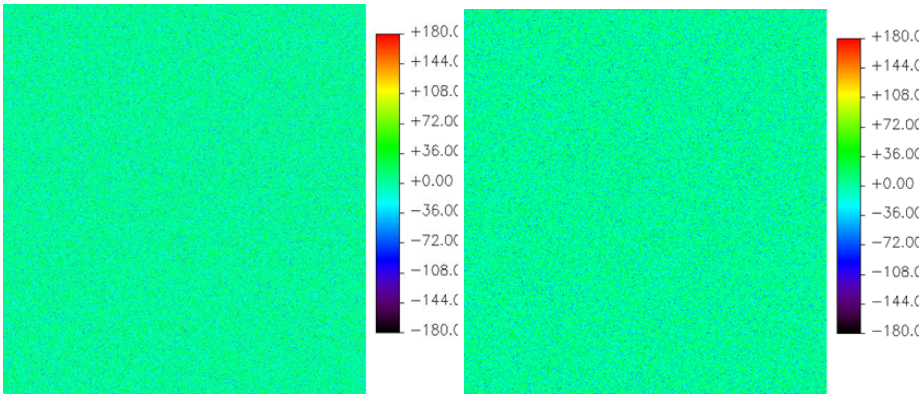

(c) Phase difference baseline 28 m (d) Phase difference baseline 57 m

Figure .16: Differences between the phase obtained with the dual frequency approach of the RG algorithm and the initial one.

Bibliography

[1] Søren Nørvang Madsen, Niels Skou, Kim Woelders, and Johan Granholm, "Emisar single pass topographic sar interferometer modes," in *Geoscience and Remote Sensing Symposium, 1996. IGARSS'96.'Remote Sensing for a Sustainable Future.', International*. IEEE, 1996, vol. 1, pp. 674–676.

[2] Richard Bamler and Philipp Hartl, "Synthetic aperture radar interferometry," *Inverse problems*, vol. 14, no. 4, pp. R1, 1998.

[3] Pau Prats-Iraola, *Airbone Differential SAR Interferometry*, Ph.D. thesis, Universitat Politècnica de Catalunya, 2006.

[4] Mónica Malén Denham, Javier A Areta, Isidoro Vaquila, and Fernando Gustavo Tinetti, "Procesamiento de señales sar: algoritmo rda para gp-gpu," in *XVIII Congreso Argentino de Ciencias de la Computación*, 2013.

[5] GW Davidson, IG Cumming, and MR Ito, "A chirp scaling approach for processing squint mode sar data," *Aerospace and Electronic Systems, IEEE Transactions on*, vol. 32, no. 1, pp. 121–133, 1996.

[6] DLR, "http://www.dlr.de/hr/en/desktopdefault.aspx/tabid-2326/3776$_r ead-$5679/," 27/08/2013.

[7] DLR, "http://www.dlr.de/hr/en/desktopdefault.aspx/tabid-2326/3776$_r ead-$5691/," 27/08/2013.

[8] Curtis W Chen and Howard A Zebker, "Phase unwrapping for large sar interferograms: statistical segmentation and generalized network models," *Geoscience and Remote Sensing, IEEE Transactions on*, vol. 40, no. 8, pp. 1709–1719, 2002.

[9] José M Bioucas-Dias and Gonçalo Valadão, "Phase unwrapping via graph cuts," *Image Processing, IEEE Transactions on*, vol. 16, no. 3, pp. 698–709, 2007.

[10] Agnes Benedek, Rafael Panzone, et al., "The space $l\backslash$ sp {p} $, with mixed norm,"$ $Duke Mathematical Journal, vol. 28, no. 3, pp. 301 - -324, 1961.$

[11] David L Fried, "Least-square fitting a wave-front distortion estimate to an array of phase-difference measurements," *JOSA*, vol. 67, no. 3, pp. 370–375, 1977.

[12] Richard M Goldstein, Howard A Zebker, and Charles L Werner, "Satellite radar interferometry: Two-dimensional phase unwrapping," *Radio Science*, vol. 23, no. 4, pp. 713–720, 1988.

[13] Dennis C Ghiglia and Mark D Pritt, *Two-dimensional phase unwrapping: theory, algorithms, and software*, Wiley New York:, 1998.

[14] Yuri Boykov and Vladimir Kolmogorov, "An experimental comparison of min-cut/max-flow algorithms for energy minimization in vision," *Pattern Analysis and Machine Intelligence, IEEE Transactions on*, vol. 26, no. 9, pp. 1124–1137, 2004.

[15] Dennis C Ghiglia and Louis A Romero, "Minimum l< sup> p</sup>-norm two-dimensional phase unwrapping," *JOSA A*, vol. 13, no. 10, pp. 1999–2013, 1996.

[16] Curtis W Chen and Howard A Zebker, "Network approaches to two-dimensional phase unwrapping: intractability and two new algorithms," *JOSA A*, vol. 17, no. 3, pp. 401–414, 2000.

[17] Curtis W Chen and Howard A Zebker, "Two-dimensional phase unwrapping with use of statistical models for cost functions in nonlinear optimization," *JOSA A*, vol. 18, no. 2, pp. 338–351, 2001.

[18] Wei Xu and Ian Cumming, "A region-growing algorithm for insar phase unwrapping," *Geoscience and Remote Sensing, IEEE Transactions on*, vol. 37, no. 1, pp. 124–134, 1999.

[19] Vito Pascazio and Gilda Schirinzi, "Multifrequency insar height reconstruction through maximum likelihood estimation of local planes parameters," *Image Processing, IEEE Transactions on*, vol. 11, no. 12, pp. 1478–1489, 2002.

[20] Giampaolo Ferraioli, Aymen Shabou, Florence Tupin, and Vito Pascazio, "Multichannel phase unwrapping with graph cuts," *Geoscience and Remote Sensing Letters, IEEE*, vol. 6, no. 3, pp. 562–566, 2009.

[21] Leonid I Rudin, Stanley Osher, and Emad Fatemi, "Nonlinear total variation based noise removal algorithms," *Physica D: Nonlinear Phenomena*, vol. 60, no. 1, pp. 259–268, 1992.

[22] Pau Prats, Andreas Reigber, Jordi J Mallorqui, and Antoni Broquetas, "Efficient detection and correction of residual motion errors in airborne sar interferometry," in *Geoscience and Remote Sensing Symposium, 2004. IGARSS'04. Proceedings. 2004 IEEE International*. IEEE, 2004, vol. 2, pp. 992–995.

[23] Ridha Touzi, Armand Lopes, Jérôme Bruniquel, and PARIS W Vachon, "Coherence estimation for sar imagery," *Geoscience and Remote Sensing, IEEE Transactions on*, vol. 37, no. 1, pp. 135–149, 1999.

[24] Yongjian Yu and Scott T Acton, "Speckle reducing anisotropic diffusion," *Image Processing, IEEE Transactions on*, vol. 11, no. 11, pp. 1260–1270, 2002.

[25] Per Christian Hansen, "Analysis of discrete ill-posed problems by means of the l-curve," *SIAM review*, vol. 34, no. 4, pp. 561–580, 1992.

[26] Muriel Pinheiro, Andreas Reigber, Rolf Scheiber, and Marc Jaeger, "Dem generation using large-baseline airborne insar," in *EUSAR 2014; 10th European Conference on Synthetic Aperture Radar; Proceedings of*. VDE, 2014, pp. 1–4.